Analysis of Pore Collapse and Shear-Enhanced Compaction in Hydrocarbon Reservoirs Using Coupled Poro-Elastoplasticity and Permeability

Manouchehr Sanei[a], Omar Durán[b], Philippe R.B. Devloo[c], Erick S.R. Santos[d]

[a]*Mechanical Engineering Department (FEM) - Petroleum Engineering Division, University of Campinas, Campinas, SP, Brazil*
[b]*Centre d'Enseignement et de Recherche en Mathématiques et Calcul scientifique, CERMICS (ENPC), Université Paris-Est, Paris, France*
[c]*Civil Engineering Department (FEC), University of Campinas, Campinas, SP, Brazil*
[d]*Research and Development Center (Cenpes), Petrobras, Rio de Janeiro, RJ, Brazil*

Abstract

The withdrawal of fluid from a reservoir results in a decline of the fluid pressure followed by a consequent change in stress state in porous rocks. Stress change may cause irreversible deformation and compaction. Such compaction is generally the result of pore collapse and shear-enhanced compaction caused by changes at a microscopic level in the porous rocks. Pore collapse and shear-enhanced compaction are considered as potential problems during reservoir production and drilling operations. The purpose of this paper is to analyze the pore collapse and shear-enhanced compaction in hydrocarbon reservoirs using coupled poro-elastoplasticity and permeability. This coupling is implemented using a sequentially coupled scheme with a fixed stress split. In this coupling, the poro-elastoplasticity analysis includes the linear component based on Biot's theory and the nonlinear component based on a cap plasticity model. The fluid flow formulation is defined by Darcy's law, including nonlinear permeability model. The numerical approximation is implemented using continuous finite element approximations for rock deformation and mixed finite element approximation for pore pressure and flux. Several numerical simulations are performed to indicate the onset

Email address: Corresponding author: manouchehr.sanei@gmail.com (Manouchehr Sanei)

of pore collapse and shear-enhanced compaction and evaluate their effects on reservoir performance.

Keywords: Pore Collapse, Shear-Enhanced Compaction, Coupled Poro-Elastoplasticity and Permeability, Finite Element Analysis.

---

1. Introduction

Surface subsidence over producing hydrocarbons, caused by a reduction of fluid pressure and consequent compaction of reservoir rocks, enhances problems for drilling operation and reservoir production (Simon et al., 1982; Sulak & Danielsen, 1988; Gurevich & Chilingarian, 1993). Historically, there are many well-known cases of surface subsidence and reservoir compaction, such as Ekofisk oil fields in North Sea, Wilmington in California, and Lagunillas fields in Venezuela. Compaction can occur as the effects of mechanical and chemical process, which is a considerable challenge to understand during the long-term reservoir production (Ostermeier, 2001). The chemical compaction commonly becomes the dominant process at higher depths and mechanical compaction governs the response at lower depths (Poulet & Veveakis, 2016).

In the mechanical regime, such compaction is due to pore collapse and shear-enhanced compaction, which they can change the strain state of reservoir and then, causes to reduce porosity and permeability (Brace, 1978). Reduction of porosity and permeability may lead to reduce oil production that can have a considerable influence on the further recovery of hydrocarbons (Xiong et al., 2018). This phenomenon is more common in weakly cemented, poorly-consolidated, overpressured reservoirs, high porosity and low permeability rock (Hoek, 2016). The onset of pore collapse and shear-enhanced compaction typically depends on the properties of the reservoir, such as depth and thickness of the reservoir, initial stress state, pore pressure, and the reservoir stress path (Zoback, 2007). However, these phenomena have been analyzed, they are not considered in the conventional reservoir simulation (Wan, 2002).

Pore collapse has been studied widely in the literature, such studies have shown macroscopically the pore collapse phenomena in the laboratory, e.g., (Blanton, 1981; Johnson et al., 1988) and such researchers have indicated the microscopic changes because of pore collapse in reservoir rocks (Addis, 1987; Abdulraheem et al., 1994). Heiland (2003) expressed that with an increase of hydrostatic stress, the porosity and permeability reduce continuously until

the initiation of pore collapse which the permeability reduction undergoes a sharp decline. Moreover, Coelho (2003) indicated that a cap plasticity model is able to clearly indicate the pore collapse of porous rocks.

Shear-enhanced compaction has been studied by several researchers, such as Schock et al. (1973); Curran & Carroll (1979) who presented that the shear-enhanced compaction can be induced by the application of a nonhydrostatic stress. Tembe et al. (2008) indicated the onset of shear-enhanced compaction by using acoustic emission. Baud et al. (2006) expressed that the onset of shear-enhanced compaction can be described using cap plasticity model. Also, Jongerius (2016) expressed that a large reduction in porosity and permeability is observed once the shear-enhanced compaction is started.

To analyze pore collapse and shear-enhanced compaction in hydrocarbon reservoirs and its impact on reservoir performance, the coupled poroelastoplasticity and fluid flow is required. This coupling is complex, because of the complexity of the physics and of the complicated geometry of the reservoir rock (Lewis et al., 2003). Poro-elastoplasticity is usually presented through the elastoplasticity constitutive models. The implementation of the elastoplasticity models in finite element demands the use of numerical integration algorithms for presenting the incremental evolution of stresses and hardening parameters (Borja & Lee, 1990).

Originally, the coupled fluid flow and deformation in porous media was first described by Terzaghi (1925). He proposed the concept of effective stress for incompressible solid grains. His one-dimensional consolidation theory has hitherto used in subsidence problems. Later, the extension of the Terzaghi's work to the three-dimensional was formulated by Biot (1941b,a) in a framework consistent with the basic principles of continuum mechanics. Subsequently, he developed the poroelasticity theory for anisotropic and nonlinear materials (Biot, 1955; Biot & Willis, 1957; Biot, 1962, 1973). Also, the development of consolidation theories of complex models dealing with nonlinear problems and thermal effect was done by (Small et al., 1976; Coussy, 1989; Lewis & Schrefler, 1998). Moreover, the extension of poroelasticity to poroelastoplasticity was devleoped by (Coussy, 1995). The following publications deal with the modeling of coupled fluid flow and deformation: (Settari & Mourits, 1998; Thomas et al., 2002; Phillips & Wheeler, 2007; Wei & Zhang, 2010; Sanei et al., 2017; Jiang & Yang, 2018; Duŕan et al., 2019).

There are three approaches to model the coupling of fluid flow and deformation in porous media: fully coupled, sequentially coupled, and loosely coupled (Settari & Walters, 2001; Dean et al., 2006). In the fully coupled

scheme, the governing equations of fluid flow and deformation are solved simultaneously at every time step. This method is unconditionally stable but it is computationally expensive (Gutierrez & Lewis, 2002; Jha & Juanes, 2007; Pan, 2009). Different sequentially coupled schemes exist depending on which variables are kept constant and the order in which the sequential stages are executed. For example, by fixing the variation of total volumetric stress for reservoir equations and the fluid pressure for geomechanics, one solves the flow problem first, and then uses computed pressure approximation to solve the deformation problem (Armero & Simo, 1992; Tran et al., 2005; Wheeler & Gai, 2007). This sequential method is iterated until the solution converges to the desired tolerance. This approach is more efficient than the fully coupled solution process either for linear and nonlinear poromechanics problems. In the loosely coupled scheme, the coupling between flow and deformation is solved only after a certain number of flow time steps (Bevillon & Masson, 2000; Minkoff et al., 2003; Samier et al., 2008). The loosely coupled scheme is only conditionally stable and requires the choice of a criterion to determine when to update the deformation response.

Due to the high computational cost of the fully coupled scheme, the sequential solution schemes is generally more efficient than the fully coupled approach. Kim et al. (2011a,b) proposed four types of sequential coupled schemes, such as drained split, undrained split, fixed strain split, and fixed stress split. Kim et al. (2011c) concluded that among sequential schemes the fixed stress split strategy is unconditionally stable and has better convergence properties. The fixed stress split scheme consists of solving first the flow problem while freezing the volumetric mean total stress, and then the mechanical part is solved from the values computed at the previous flow step.

In this article, the impact of pore collapse and shear-enhanced compaction on the reservoir performance is analyzed using a sequential numerical scheme with a fixed stress split for the coupled poro-elastoplasticity and permeability. To define the elastoplastic deformation, the conservation of momentum, Biot's law and DiMaggio-Sandler cap plasticity model are used. To represent fluid flow, the conservation of mass and Darcy's law with considering nonlinear Davies permeability are employed. The numerical approximation uses continuous Galerkin finite element for displacement and mixed finite element for pore pressure and flux. The onset of pore collapse and shear-enhanced compaction from the numerical results with respect to commonly used approaches is indicated by three methods: firstly using the DiMaggio-

Sandler cap plasticity model, secondly using the compaction model of Wong, and thirdly using the shear bands of Rudnicki. The implementation of the present study is done using the NeoPZ library, which is an object-oriented scientific computational environment, providing a framework for developing finite element schemes (Devloo, 1997, 2000).

2. Article Contributions

The major contributions of this article are:

- The sequential numerical scheme is proposed to implement a coupled poro-elastoplasticity and permeability.
- The effect of pore collapse and shear-enhanced compaction on the reservoir performance is analyzed using the coupled poro-elastoplasticity and permeability, in which the DiMaggio-Sandler cap plasticity and nonlinear Davies permeability model are used;
- The onset of pore collapse and shear-enhanced compaction from the numerical results with respect to commonly used approaches is indicated by three methods: firstly using the DiMaggio-Sandler cap plasticity model, second a compaction model of Wong, and third shear bands of Rudnicki;
- Several models in 2D and 3D simulations are performed to indicate the impact of pore collapse and shear-enhanced compaction, especially the onset of them applied to hydrocarbon reservoirs.

3. Model Formulation

The governing equations for coupled poro-elastoplasticity and permeability are composed for a set of conservation laws and constitutive laws. The conservation equations are related to momentum and mass.

3.1. Momentum Conservation

The conservation of momentum under the quasi-static assumption is expressed as (Rudnicki, 1986):

$$\operatorname{div}\left(\boldsymbol{\sigma}_t - \boldsymbol{\sigma}_t^{\circ}\right) = 0 \tag{1}$$

where $\mathrm{div}(\cdot)$ [m^{-1}] is the divergence operator on the deform configuration, $\boldsymbol{\sigma}_t^\circ$ and $\boldsymbol{\sigma}_t$ [MPa] are the initial and the current Cauchy total stress tensor, respectively. The corresponding initial (referred with the superscript $(\cdot)^\circ$) and boundary conditions of momentum conservation are:

$$I.C. = \begin{cases} p = & p^\circ \ on\ \Omega \\ \mathbf{u} = & \mathbf{u}^\circ \ on\ \Omega \end{cases} \quad B.C. = \begin{cases} \boldsymbol{\sigma}_t \cdot \mathbf{n} & = \mathbf{t} \ on \ \Gamma_N^{\boldsymbol{\sigma}_t} \\ \mathbf{u} & = \mathbf{u}_D \ on \ \Gamma_D^{\mathbf{u}} \end{cases} \tag{2}$$

The momentum conservation in equation (1) is defined in terms of Cauchy effective stress tensor as:

$$\mathrm{div}\left(\boldsymbol{\sigma} - \boldsymbol{\sigma}^\circ - \alpha\left(p - p^\circ\right)\mathbf{I}\right) = 0 \tag{3}$$

where $\boldsymbol{\sigma}^\circ$ and $\boldsymbol{\sigma}$ are the initial and current Cauchy effective stress [MPa], respectively. α is the Biot's coefficient, $\mathbf{I}$ is the second rank identity tensor, p° and p are the initial and current fluid pressure [MPa], respectively. The effective stress $\boldsymbol{\sigma}$ is determined by linear stress-strain relationship, as:

$$\boldsymbol{\sigma} - \boldsymbol{\sigma}^\circ = 2\mu\left(\boldsymbol{\epsilon}_e - \boldsymbol{\epsilon}_e^\circ\right) + \lambda tr\left(\boldsymbol{\epsilon}_e - \boldsymbol{\epsilon}_e^\circ\right)\mathbf{I} \tag{4}$$

where $\boldsymbol{\epsilon}_e$ is the elastic strain. The parameters μ and λ are the Lamé constants [MPa].

3.2. Mass Conservation

For a slightly compressible fluid, the mass conservation is defined by (Rudnicki, 1986) as follows:

$$\frac{\partial\left(\phi\rho_f\right)}{\partial t} + \mathrm{div}\left(\mathbf{q}\right) = 0 \tag{5}$$

where $\mathbf{q} = \rho_f \mathbf{v}_f$ is the flux [$\mathrm{kg\,s^{-1}\,m^{-2}}$], in which $\mathbf{v}_f$ [$\mathrm{m\,s^{-1}}$] is the fluid velocity. The corresponding initial and boundary conditions of mass conservation are:

$$\mathrm{I.C.} = \left\{ p = \ p^\circ \ on\ \Omega \right. \qquad \mathrm{B.C.} = \begin{cases} \mathbf{q} \cdot \mathbf{n} & = & q_n \ \mathrm{on} \ \Gamma_N^{\mathbf{q}} \\ p & = & p_D \ \mathrm{on} \ \Gamma_D^p \end{cases} \tag{6}$$

The fluid velocity in equation (5) is described by the Darcy's law:

$$\mathbf{v}_f = -\frac{\mathbf{K}}{\eta}\nabla p \tag{7}$$

where η is the fluid dynamic viscosity [Pa s], $\mathbf{K}$ is the absolute permeability tensor [m^{-2}], which is expressed as $\mathbf{K} = \kappa\, I$, in which κ is defined using the nonlinear Davies permeability model, as follows (Davies & Davies, 1999):

$$\kappa = \kappa^{\circ} \exp\left[\mathcal{Z}\left(\frac{\phi}{\phi^{\circ}} - 1\right)\right] \tag{8}$$

$\mathcal{Z}$ is the permeability coefficient. k° and k are the initial and current permeability [m^{-2}], respectively. ϕ° and ϕ are the initial and current porosity, respectively. The Lagrangian porosity is (Kim et al., 2011b; Coussy, 2004):

$$\phi = \phi^{\circ} + \alpha\left(\epsilon_{ev} - \epsilon_{ev}^{\circ}\right) + \phi_p - \phi_p^{\circ} + S\left(p - p^{\circ}\right) \tag{9}$$

where $S = \left(\left(1-\alpha\right)\left(\alpha - \phi^{\circ}\right)\right)/K_{dr}$, in which K_{dr} [MPa] is the elastic rock bulk modulus in drained conditions. ϕ_p is the plastic porosity and it is:

$$\phi_p = \alpha_p \epsilon_{pv} \tag{10}$$

where ϵ_{pv} is the plastic volumetric strain. The parameter α_p is the nonlinear Biot's coefficient and shares the same restrictions of α, i.e. $\phi^{\circ} \leq \alpha_p \leq 1$ (Coussy, 2004; Bui et al., 2016; da Silva et al., 2018). Experimental results support the fact that $\alpha \neq \alpha_p$ (Xie & Shao, 2015). However, many researchers (Zhou et al., 2008; Kim et al., 2011b,c) assume that $\alpha = \alpha_p$. In this research, for simplicity $\alpha = \alpha_p$ is considered. The volumetric elastic strain ϵ_{ev} can be related to volumetric total stress $\sigma_{tv} = tr\left(\boldsymbol{\sigma}_t\right)/3$ as:

$$\left(\sigma_{tv} - \sigma_{tv}^{\circ}\right) + \alpha\left(p - p^{\circ}\right) = K_{dr}\left(\epsilon_{ev} - \epsilon_{ev}^{\circ}\right) \tag{11}$$

By inserting equation (11) into equation (9) and considering $S_e = S + \phi^{\circ} c_f$, an alternative expression for $(\phi\rho_f)$ is obtained (Kim et al., 2012), as:

$$\phi\rho_f = \rho_f^{\circ}\left(\phi^{\circ} + \frac{\alpha}{K_{dr}}\left(\sigma_{tv} - \sigma_{tv}^{\circ}\right) + \phi_p - \phi_p^{\circ} + \left(S_e + \frac{\alpha^2}{K_{dr}}\right)\left(p - p^{\circ}\right)\right) \tag{12}$$

where S_e is the inverse of Biot's modulus M [MPa], c_f is the fluid compressibility. ρ_f° and ρ_f are the initial and current fluid density [$\mathrm{kg\,m}^{-3}$], respectively. σ_{tv}° and σ_{tv} are the initial and current volumetric total stress [MPa], respectively.

3.3. Elastoplastic Constitutive Models

A nonlinear elastoplastic model is described by the theory of elastoplasticity, when a material undergoes an irreversible deformations. The total strain tensor $\boldsymbol{\epsilon}$ is decomposed into two parts (de Souza Neto et al., 2008):

$$\boldsymbol{\epsilon} = \boldsymbol{\epsilon}_e + \boldsymbol{\epsilon}_p \tag{13}$$

where $\boldsymbol{\epsilon}_e$ is the elastic strain and $\boldsymbol{\epsilon}_p$ is the plastic strain. The elastic strain is reversible and the plastic strain represents a permanent (i.e. irreversible) deformation (de Souza Neto et al., 2008). The total strain is defined in terms of displacement $\mathbf{u}$ as:

$$\boldsymbol{\epsilon} = \frac{1}{2}\left(\nabla\mathbf{u} + \nabla^T\mathbf{u}\right) \tag{14}$$

The elastoplastic deformation is mathematically described by four fundamental axioms (de Souza Neto et al., 2008):

Elastic law. The elastic law can be defined by using the linear stress-strain relationship expressed by equation (4).

Yield criterion. Describes the elastic limit and the plastic part through a plasticity yield function $\Phi = \Phi(\boldsymbol{\sigma}, \mathbf{A})$, where $\mathbf{A} = \bar{\rho}\partial\mathbf{F}^p/\partial\chi$ is the hardening thermodynamic force, $\mathbf{F}^p$ is the plastic part of Helmholtz free energy $\mathbf{F}$, and χ is the hardening variable. The plasticity function assumes negative values in the elastic part and null values in the plastic part (Kossa, 2011).

Flow rule. Assumes the existence of a plastic potential function $\Psi = \Psi(\boldsymbol{\sigma}, \mathbf{A})$, which specifies how the plastic deformation tensor evolves in the plasticity process $\dot{\epsilon}_p = \dot{\gamma}\mathbf{N}$, in which $\mathbf{N}(\boldsymbol{\sigma}, \mathbf{A}) = \partial\Psi/\partial\boldsymbol{\sigma}$ is the flow direction and $\dot{\gamma}$ is the plastic multiplier. The flow rule is called associative if the plastic potential function equals to yield function, namely $\Psi = \Phi$ (Davis & Selvadurai, 2002).

Hardening law. Specifies how the internal damage variable $\dot{\chi} = \dot{\gamma}H$ evolves, in which, $H(\boldsymbol{\sigma}, \mathbf{A}) = -\partial\Psi/\partial\mathbf{A}$ is the hardening modulus.

3.3.1. Time Evolution in Elastoplasticity

The time evolution in elastoplasticity is formed by giving the elastic strain $\boldsymbol{\epsilon}_e^{n-1}$, the plastic strain $\boldsymbol{\epsilon}_p^{n-1}$, and the hardening variable χ^{n-1} at a (pseudo) time step t^{n-1}, and also given a prescribed incremental strain tensor $\Delta\boldsymbol{\epsilon}$ for the time interval $[t^{n-1}, t^n]$ in order to find the following system of algebraic equations at a time-step t^n (de Souza Neto et al., 2008):

$$\begin{array}{rcl} \boldsymbol{\epsilon}_e^n & = & \boldsymbol{\epsilon}_e^{n-1} + \Delta\boldsymbol{\epsilon} - \Delta\gamma\, \boldsymbol{N}\left(\boldsymbol{\sigma}^n, \mathbf{A}^n\right) \\ \chi^n & = & \chi^{n-1} + \Delta\gamma\, H\left(\boldsymbol{\sigma}^n, \mathbf{A}^n\right) \end{array} \tag{15}$$

for the unknowns $\boldsymbol{\epsilon}_e^n$, χ^n and incremental of plastic multiplier $\Delta\gamma$, it is subjected to the restrictions:

$$\Delta\gamma \geq 0,\ \Phi\left(\boldsymbol{\sigma}^n, \mathbf{A}^n\right) \leq 0,\ \Delta\gamma\, \Phi\left(\boldsymbol{\sigma}^n, \mathbf{A}^n\right) = 0 \tag{16}$$

Solving the elastoplastic problem occurs in two steps. First an elastic response is computed (i.e. elastic trial step), where $\Delta\gamma = 0$ leading to the elastic trial stress $\boldsymbol{\epsilon}_{e_{trial}}^n = \boldsymbol{\epsilon}_e^{n-1} + \Delta\boldsymbol{\epsilon}$ and hardening variable $\chi_{trial}^n = \chi^{n-1}$. Then, $\boldsymbol{\sigma}_{trial}^n$ and $\Phi\left(\boldsymbol{\sigma}_{trial}^n, \mathbf{A}_{trial}^n\right)$ are computed as a function of $\boldsymbol{\epsilon}_{e_{trial}}^n$. If $\Phi\left(\boldsymbol{\sigma}_{trial}^n, \mathbf{A}_{trial}^n\right) \leq 0$, the elastic response is a valid solution and the elasto plastic variables are updated from the trial values $(\cdot)^n := (\cdot)_{trial}^n$. Otherwise, the return-mapping algorithm is applied and a set of nonlinear equations needs to be solved (de Souza Neto et al., 2008):

$$\begin{array}{c} \boldsymbol{\epsilon}_e^n = \boldsymbol{\epsilon}_{e_{trial}}^n - \Delta\gamma\, \boldsymbol{N}\left(\boldsymbol{\sigma}^n, \mathbf{A}^n\right) \\ \chi^n = \chi_{trial}^n + \Delta\gamma\, H\left(\boldsymbol{\sigma}^n, \mathbf{A}^n\right) \\ \Delta\gamma > 0,\ \Phi\left(\boldsymbol{\sigma}^n, \mathbf{A}^n\right) = 0 \end{array} \tag{17}$$

Once the solution $\boldsymbol{\epsilon}_e^n$ has been calculated, the plastic strain at a time step t^n can be computed as:

$$\boldsymbol{\epsilon}_p^n = \boldsymbol{\epsilon}_p^{n-1} + \Delta\boldsymbol{\epsilon} - \Delta\boldsymbol{\epsilon}_e \tag{18}$$

3.3.2. DiMaggio-Sandler Elastoplasticity Model

The DiMaggio-Sandler elastoplasticity model was presented in (DiMaggio & Sandler, 1971). It was developed to model granular soils, but can also be applied to problems relevant to the oil industry representing the behavior of rocks at depth (Cecílio et al., 2015). The yield function Φ of DiMaggio-Sandler model is defined by two functions: a failure function $F_f(I_1, \sqrt{J_2})$ and a cap function $F_c(I_1, \sqrt{J_2}, L)$:

$$\Phi = \begin{cases} F_f(I_1, \sqrt{J_2}), & I_1 > L \\ F_c(I_1, \sqrt{J_2}, L), & L \geqslant I_1 \geqslant X \end{cases} \tag{19}$$

where $L(\chi)$ is the cap position parameter [MPa], $X(\chi)$ is the current cap surface position [MPa], I_1 is the first invariant of the stress tensor [MPa], and J_2 is the second deviatoric stress tensor [MPa^2]. The expressions of the failure function and cap function are:

$$\begin{cases} F_f(I_1, \sqrt{J_2}) = \sqrt{J_2} - F_s(I_1) \\ \\ F_c(I_1, \sqrt{J_2}, L) = (\frac{I_1 - L}{R F_s(L)})^2 + (\frac{\sqrt{J_2}}{F_s(L)})^2 - 1 \end{cases} \tag{20}$$

with,

$$L(\chi) = \begin{cases} \chi & if \quad \chi < 0 \\ 0 & if \quad \chi \geq 0 \end{cases} \tag{21}$$

$$F_s(\iota) = A - C \exp(B\,\iota) \qquad X = L - R F_s(L) \tag{22}$$

where A [MPa], B [MPa^{-1}], C [MPa] are material property constants and R is the ratio of principal ellipse radii of the cap surface. A typical *2D* profile of DiMaggio-Sandler yield surface is plotted in Figure 1.

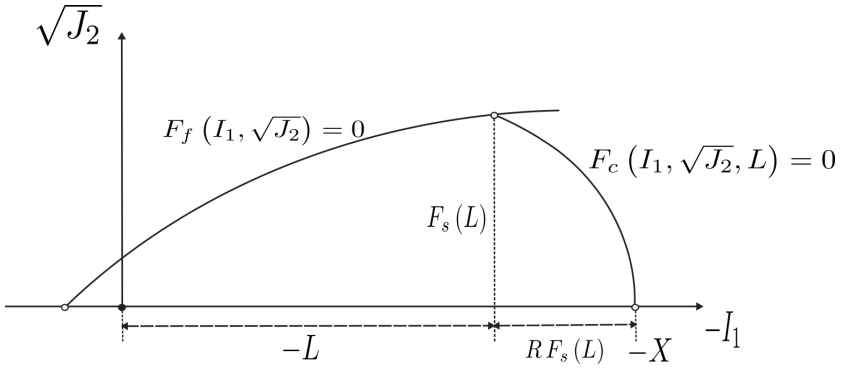

Figure 1. DiMaggio-Sandler plastic yield profile in the $(I_1, \sqrt{J_2})$ plane (Sandler & Rubin, 1979).

The hardening parameter χ of DiMaggio-Sandler cap model is defined through a functional of $X(\chi)$ and volumetric plastic strain ϵ_{pv} as follows (Fossum et al., 1995):

$$\epsilon_{pv} = W\left(\exp[D\left(X - X_{\circ}\right)] - 1\right) \tag{23}$$

where $X_{\circ}$ is the initial cap position [MPa]. D [MPa^{-1}] and W are the material properties constants. The yield surface of DiMaggio-Sandler in *3D* is illustrated in Figure 2.

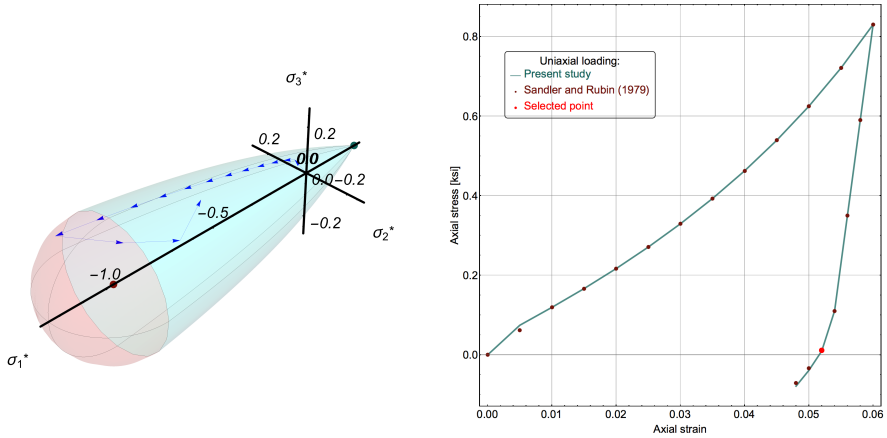

Figure 2. (left) DiMaggio-Sandler plasticity yield criterion in which failure function part is with a green color and cap function is with a red color, and (right) a comparison between numerical model of DiMaggio-Sandler with the experimental data reported by (Sandler & Rubin, 1979); the arrow with a blue color in middle shows the evolution of elastoplastic model which is represented here by a point with a red color.

3.4. Strong Statement of Coupling

The strong statement of the coupling is presented using the conservation laws given in equations (3) and (5), as follows:

$$\begin{cases} \operatorname{div}\left(\boldsymbol{\sigma} - \boldsymbol{\sigma}^{\circ} - \alpha\left(p - p^{\circ}\right)\mathbf{I}\right) = 0 \\ \\ \dfrac{\partial\left(\phi\rho_f\right)}{\partial t} + \operatorname{div}\left(\mathbf{q}\right) = 0 \end{cases} \tag{24}$$

It is completed by considering the equations (4) and (7), namely:

$$\begin{cases} \boldsymbol{\sigma} - \boldsymbol{\sigma}^{\circ} = 2\mu\left(\boldsymbol{\epsilon}_e - \boldsymbol{\epsilon}_e^{\circ}\right) + \lambda tr\left(\boldsymbol{\epsilon}_e - \boldsymbol{\epsilon}_e^{\circ}\right)\mathbf{I} \\ \\ \mathbf{v}_f = -\dfrac{\mathbf{K}}{\eta}\nabla p \end{cases} \tag{25}$$

The strong statement is incorporated with Dirichlet and Neumann boundary conditions in the equations (2) and (6).

3.5. Weak Statement of Coupling

The weak statement of the coupling is presented by using one field $\mathbf{u}$ as state variable for the elastoplastic problem and two fields $\mathbf{q}$ and p for the Darcy's flow problem, as:

$$\begin{cases} \int_{\Omega} \left(\boldsymbol{\sigma}^{n} - \boldsymbol{\sigma}^{\circ} - \alpha \left(p^{n} - p^{\circ}\right) \mathbf{I}\right) \cdot \boldsymbol{\epsilon}\left(\boldsymbol{\phi}_{u}\right) \, d\Omega - \int_{\Gamma_{N}} \left(\mathbf{t}^{n} - \mathbf{t}^{\circ}\right) \cdot \boldsymbol{\phi}_{u} \, d\Gamma = 0 \\ \int_{\Omega} \left(\rho_{f}^{n} \frac{\kappa^{n} \mathbf{I}}{\eta}\right)^{-1} \mathbf{q}^{n} \cdot \boldsymbol{\phi}_{q} \, d\Omega + \int_{\Gamma_{D}} p^{n} \cdot \boldsymbol{\phi}_{q} \cdot \mathbf{n} \, d\Gamma - \int_{\Omega} p^{n} \cdot \operatorname{div}\left(\boldsymbol{\phi}_{q}\right) \, d\Omega = 0 \\ \int_{\Omega} \operatorname{div}\left(\mathbf{q}^{n}\right) \cdot \phi_{p} \, d\Omega + \int_{\Omega} \left(\frac{\phi \rho_{f}|^{n} - \phi \rho_{f}|^{n-1}}{\delta t}\right) \cdot \phi_{p} \, d\Omega = 0 \end{cases} \tag{26}$$

where Ω is the domain, Γ is the boundary and $\boldsymbol{\phi}_{u}$, $\boldsymbol{\phi}_{q}$, ϕ_{p} are the test functions. The weak statement is incorporated with Dirichlet and Neumann boundary conditions in the equations (2) and (6).

3.6. Sequential Coupled Scheme

The sequential coupled scheme is a common approach to handle coupled flow, and transport equations for multiphase flow in porous media (Jiang & Tchelepi, 2018). The schematic of the sequential coupled scheme is shown in Figure 3. This scheme is applied with the fixed stress split as a robust procedure to approximate solutions of nonlinear equations (Kim, 2010).

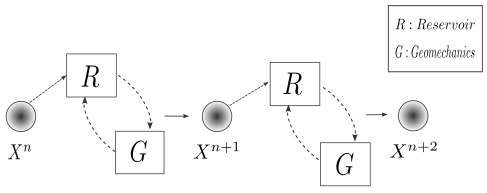

Figure 3. Schematics of the sequential coupled scheme (Kim, 2010).

The sequential scheme is used to approximate the time dependent problem of coupled poro-elastoplastic and permeability. The scheme computes a new state $(\mathbf{u}, \mathbf{q}, p)^{m}$ in a time step of size Δt, by starting an external

loop with counter $m \to 1$ to execute a sequence of two nonlinear solvers (a fluid flow module and a poro-elastoplastic module with internal loops that counter n). In order to describe the implementation of sequential coupled scheme, the change in porosity over a timestep (as defined by equation (12)) is decomposed in two parts $\delta\phi = \phi - \phi^{\circ}$ as (Kim et al., 2011b):

$$\phi = \phi^{\circ} + \delta\phi \tag{27}$$

$$\begin{cases} \delta\phi = \delta\phi_{pore} + \overbrace{\delta\phi_{matrix}}^{\delta\phi_f^* + \delta\phi_s^*} \\ \delta\phi = \delta\phi_{pore} + \delta\phi_f^* + \delta\phi_s^* \end{cases} \tag{28}$$

where

$$\begin{cases} \delta\phi_{pore} & = S\left(p - p^{\circ}\right) \\ \delta\phi_{matrix} & = \underbrace{\dfrac{\alpha^2}{K_{dr}}\left(p - p^{\circ}\right)}_{\delta\phi_f^*} + \underbrace{\dfrac{\alpha}{K_{dr}}\left(\sigma_{tv} - \sigma_{tv}^{\circ}\right) + \phi_p - \phi_p^{\circ}}_{\delta\phi_s^*} \end{cases} \tag{29}$$

where $\delta\phi_f^*$ and $\delta\phi_s^*$ are the matrix parts of porosity change. The variation of the fluid content expressed by equation (29) is computed using two stages (Settari & Mourits, 1998; Mikelić & Wheeler, 2012; Duŕan et al., 2019):

1. For the fluid flow module the variation of $\delta\phi_{pore}$ and $\delta\phi_f^*$ are computed and the $\delta\phi_s^*$ is considered constant;
2. For the poro-elastoplastic module $\delta\phi_s^*$ is updated.

At the first step, it is set to ${\delta\phi_s^*}^{m-1} \to 0$ and add the $\left(\alpha^{n-1}\right)^2/K_{dr}$ to the fluid flow module, and the equation is solved as follows:

- **Fluid Flow Module:** by allowing to compute implicitly $p^{n,m}$, while the total volumetric stress and the plastic porosity are constant during solving the fluid flow iterations, the porosity $\phi^{n,m}$ is approximated as:

$$\begin{cases} \phi^{n,m} \approx \phi^{\circ} + \delta\phi_{pore}^{n,m} + {\delta\phi_f^*}^{n-1,m} + {\delta\phi_s^*}^{m-1} \\ \phi^{n,m} \approx \phi^{\circ} + \underbrace{S\left(p^{n,m} - p^{\circ}\right)}_{\delta\phi_{pore}} + \underbrace{\left(\left(\alpha^{n-1}\right)^2/K_{dr}\right)\left(p^{n,m} - p^{\circ}\right)}_{\delta\phi_f^*} + \underbrace{{\delta\phi_p^*}^{m-1}}_{\delta\phi_s^*} \end{cases} \tag{30}$$

Consecutively, the pressure is transferred to the poro-elastoplastic module and the equation is solved as follows:

- **Poro-Elastoplastic Module:** Once the pressure $p^{n,m}$ is determined, then the term $\delta\phi_s^{*\,m}$ is computed implicitly using the expression:

$$\delta\phi_s^{*\,m} = \frac{\left(\alpha^{n-1}\right)^2}{K_{dr}}\left(\sigma_{tv}^{n,m} - \sigma_{tv}^{\circ}\right) + \phi_p^{n,m} - \phi_p^{\circ} \tag{31}$$

It is considered to maintain the Biot coefficient constant during a timestep iteration and only between timesteps is updated using the following expression (Kim et al., 2012):

$$\alpha = 1 - \frac{K_{dr_{ep}}}{K_s} \quad ; \quad K_{dr_{ep}} = \frac{\delta\sigma_v}{\delta\epsilon_v} \tag{32}$$

where $K_{dr_{ep}}$ [MPa] is the elastoplastic tangent bulk modulus, K_s [MPa] is the solid bulk modulus, $\delta\sigma_v$ [MPa] is volumetric effective stress variation, and $\delta\epsilon_v$ is the volumetric total strain variation.

The sequence between both fluid flow and poro-elastoplastic module is repeated until a desired stopping criteria is reached.

4. Pore Collapse and Shear-Enhanced Compaction

During production of hydrocarbon from both the unconsolidated and weakly consolidated reservoir rocks, they can undergo irreversible deformation (compaction). Such compaction is generally the results of pore collapse and shear-enhanced compaction at the microscopic level, within the rock mass. Pore collapse and shear-enhanced compaction are considered potential problems in the reservoirs. To overcome these problems, it is required to evaluate the probability of pore collapse and shear-enhanced compaction.

4.1. Constitutive Models

The theory of plasticity provides a constitutive framework for the analysis of compaction in a granular material, such as soil (Chen, 1984), porous sandstone (Wong et al., 1997), porous diatomites (A.F. & J.T., 2000), and carbonate rocks (Vajdova et al., 2004). Generally, two types of plasticity models have been applied: the cap model which was formulated by DiMaggio & Sandler (1971) that extensively applied for both soil and porous rock, and the critical state model (A. Schofield, 1968) which has been widely used in soil

mechanics. In this study, DiMaggio-Sandler cap plasticity model is applied to analyze the compaction phenomenon. The original DiMaggio-Sandler cap plasticity model in equation (20) is rewritten as follows (DiMaggio & Sandler, 1971):

$$\Phi_{ds} = \left(\frac{I_1 - L}{RF_s\left(L\right)}\right)^2 + \left(\frac{\sqrt{J_2}}{F_s\left(L\right)}\right)^2 - 1 \tag{33}$$

It corresponds to an ellipse centered at $(L, 0)$ with major and minor semi-axes of $RF_s\left(L\right)$ and $F_s\left(L\right)$. Moreover, the first stress invariant I_1 can be related to the effective mean stress P by $I_1 = -3P$ and the second invariant J_2 to the von Mises stress Q by $3J_2 = Q^2$. The DiMaggio-Sandler model can be defined on the ellipse with semiaxes $R_I = \left(RF_s\left(L\right)\right)/3$, $R_{II} = \sqrt{3}F_s\left(L\right)$, and center at $(C^t = L/3)$, which is rewritten as follows (Baud et al., 2006):

$$\Phi_{ds} = \frac{\left(P - C^t\right)^2}{R_I^2} + \frac{Q^2}{R_{II}^2} - 1 \tag{34}$$

4.2. Theoretical Model

When studying the mechanical behavior of porous materials, three effects of plastic deformation related to permeability can be recognized; pore collapse, shear-enhanced compaction, and shear-induced dilation.

4.2.1. Pore Collapse

Under the hydrostatic stress condition, the transition from elastic (pre-pore collapse) to plastic is named pore collapse (Addis & Jones, 1990), and the post-pore collapse region can be characterized by a plastic hardening model. The critical effective stress for the onset of pore collapse is denoted by P^*. In the Figure 4, that is drawn similar to experimental results of (Baud et al., 2006) in saturated sandstone, a schematic behavior of hydrostatic test and the critical stress for the onset of pore collapse, namely P^* are shown. The onset of plastic collapse is picked as the endpoint of linear evolution of volumetric strain (Nguyen et al., 2014). The onset of pore collapse P^* can be determined using two methods: firstly, an expression derived from experimental observations developed by (Zhang et al., 1990) and second, a numerical approach by applying a plasticity cap model (Coelho, 2003; Baud et al., 2006) such as the DiMaggio-Sandler and/or the modified Cam-Clay plasticity model.

- **Firstly**. The experimental model of Zhang et al. (1990) which is presented based on the Hertzian contact theory and the crack propagation mechanics. This model is a power law that describes the dependency of the critical pressure P^* with micro-structural attributes, as follows:

$$P^* \propto (\phi R_g)^n \tag{35}$$

where ϕ is the porosity, R_g is the mean grain radius, and $n = -1.5$. This model has been validated on glass beads, consolidated porous sandstones, and quartz sand by Wong et al. (1997); Karner et al. (2005).

- **Second**. Using DiMaggio-Sandler or modified Cam-Clay plasticity model to indicate the onset of pore collapse P^*, as follows:

The DiMaggio-Sandler cap plasticity model in equation (34) is rewritten in terms of normalized stresses using the critical pressure P^* as follows (Wong et al., 1997):

$$\Phi_{ds} = \frac{\left(P/P^* - \xi\right)^2}{\left(1-\xi\right)^2} + \frac{\left(Q/P^*\right)}{\delta^2} - 1 \tag{36}$$

where, $\xi = C^t/P^*$, $1 - \xi = R_I$, and $\delta = R_{II}/P^*$.

The modified Cam-Clay plasticity model is rewritten by using the critical pressure P^* as follows (Nguyen et al., 2014):

$$\Phi_{cc} = Q^2 - M^2 P \left(P^* - P\right) \tag{37}$$

Finally, the pore collapse can be described using plasticity models, as follows:

$$\Phi_{pc} = \begin{cases} \Phi_{cc} \\ or \\ \Phi_{ds} \end{cases} \tag{38}$$

The equation (38) means when the yield surface $\Phi_{pc} = 0$, the plastic deformation regime starts and this transition from elastic to plastic is named pore collapse and P^* is the critical pressure for onset of pore collapse. Moreover, the onset of pore collapse (starts a plastic strain) and post-pore collapse (evolution of plastic strain) of reservoir rocks means the deformation is irreversible and consequently the reduction of porosity and also permeability are

irreversible. Therefore pore collapse will affect reservoir performance and its occurrence can be detected using a cap plasticity model.

4.2.2. Shear-Enhanced Compaction

Under nonhydrostatic or deviatoric stress, the onset of inelastic permanent deformation in porous rock is generally associated with the onset of either permanent dilation or compaction (Rutter & Glover, 2012). The shear-enhanced compaction regime is where the nonhydrostatic stress part combines with the hydrostatic part in reaching the resistance of the pore with respect to collapse (Curran & Carroll, 1979). Shear-enhanced compaction refers to a permanent deformation of porous rock, characterized by the loss of porosity due to the pore collapse as confining pressure and/or shear stress increases beyond the yield value (Zoback, 2007). Post-yield deformation related to shear-enhanced compaction is often ductile, which leads to spreading the deformation throughout the rock mass (Underhill & Woodcock, 1987; Rutter & Glover, 2012).

Under nonhydrostatic stress condition in the cataclastic flow regime, it is observed the porosity firstly decreases up to a critical effective stress state, namely C^*, the reduction of porosity is accelerated, which is referred to the shear-enhanced compaction (Curran & Carroll, 1979; Wong et al., 1992). The C^* is the critical stress for the onset of shear-enhanced compaction and shear hardening under triaxial loading. In the Figure 4, that is drawn similar to experimental results of (Baud et al., 2006) in saturated sandstone, a schematic behavior of triaxial test and the critical stress for the onset of shear-enhanced compaction, namely C^* are displayed.

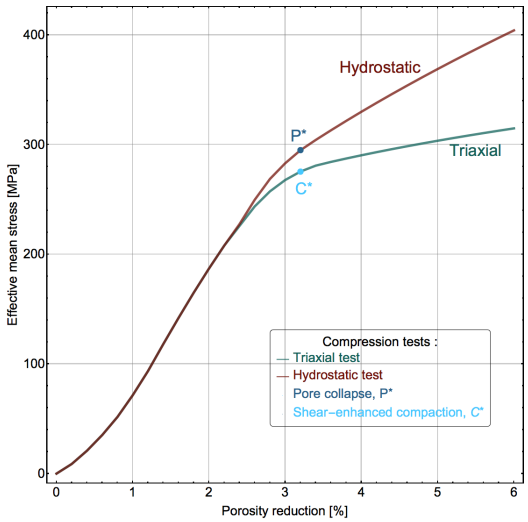

Figure 4. Schematic behavior of pore collapse and shear-enhanced compaction.

Similarly to pore collapse, three different models have been developed to represent shear-enhanced compaction C^*: firstly, a model developed by Wong et al. (1997), second, shear bands idealized by Rudnicki & Rice (1975), and third, using plasticity cap models such as the DiMaggio-Sandler cap model and/or the modified Cam-Clay model.

- **Firstly**. The compaction model of Wong et al. (1997) is based on constitutive plasticity parameters presented by Rudnicki & Rice (1975). These parameters are the internal friction parameter μ_p and the dilatancy factor β_p which can be extracted from triaxial compression test data. The dilatancy factor β_p in the article (Rudnicki & Rice, 1975) is representative for the inelastic compaction (Wong et al., 1997), as follows:

$$\beta_p = -\sqrt{3}\frac{\Delta\epsilon_p^v/\Delta\epsilon_p^a}{(3-\Delta\epsilon_p^v/\Delta\epsilon_p^a)} \tag{39}$$

where $\Delta\epsilon_p^a$ is the axial plastic strain and $\Delta\epsilon_p^v$ is the volumetric plastic strain $\Delta\epsilon_v^p$. The parameter β_p is computed from the measurement of $\Delta\epsilon_p^v/\Delta\epsilon_p^a$, provided by the laboratory test data. The difference in sign of β_p can indicate the dilatancy or compaction. Negative values of β_p indicate shear-enhanced compaction and the positive values of β_p indicate dilation regime (Baud et al., 2006).

- **Second**. The shear and compaction bands of Rudnicki & Rice (1975) can be applied to define the critical conditions for dilation, shear or compaction bands. The bands are described using the parameters β_p and μ_p as follows (Wong et al., 1997): Shear bands occurr if:

$$-\sqrt{3} \leq \mu_p + \beta_p \leq \frac{\sqrt{3}\,(2-\nu)}{(1+\nu)} \tag{40}$$

Dilation band is characterized, if:

$$\mu_p + \beta_p > \frac{\sqrt{3}\,(2-\nu)}{(1+\nu)} \tag{41}$$

Compaction band will occur, if:

$$\mu_p + \beta_p < -\sqrt{3} \tag{42}$$

where ν is the Poisson's ratio. μ_p is the friction parameter which is written as:

$$\mu_p = \frac{\sqrt{3}}{3}\frac{Q}{P} \tag{43}$$

- **Third**. The DiMaggio-Sandler or modified Cam-Clay plasticity model can be used to indicate the onset of shear-enhanced compaction C^*. The onset of shear-enhanced compaction can be obtained, similar to the plasticity models in equations (36), (37) by considering C^* as the critical mean stress, as follows:

$$\Phi_{ds} = \frac{\left(P/C^* - \xi\right)^2}{\left(1-\xi\right)^2} + \frac{\left(Q/C^*\right)}{\delta^2} - 1 \tag{44}$$

where, $\xi = C^t/C^*$, $1-\xi = R_I$ and $\delta = R_{II}/C^*$.

In addition,

$$\Phi_{cc} = Q^2 - M^2 P\left(C^* - P\right) \tag{45}$$

Finally, the shear-enhanced compaction can be presented using constitutive plasticity models, as follows:

$$\Phi_{sc} = \begin{cases} \Phi_{cc} \\ or \\ \Phi_{ds} \end{cases} \tag{46}$$

The equation (46) means when the yield surface $\Phi_{sc} = 0$, the plastic deformation regime starts and this transition in the cataclastic flow regime from elastic to plastic is named shear-enhanced compaction and C^* is the critical effective stress for onset of shear-enhanced compaction. Moreover, the onset of shear-enhanced compaction (starting point of plastic strain) and post-shear-enhanced compaction (evolution of plastic strain) of reservoir rocks means the deformation is irreversible and consequently the reduction of porosity and also permeability are irreversible. Shear-enhanced compaction can be considered as a potential problem in reservoir performance and it can be indicated using the cap plasticity model.

4.2.3. Shear-Induced Dilation

The shear stresses in porous rocks can cause either compaction or dilation in the form of shear-enhanced compaction or shear-induced dilation. In the shear-enhanced compaction mode, porosity decreases with increasing effective stress, but in shear-induced dilation, porosity increases with increasing the effective stress (Bernard et al., 2002). The shear induced dilation can be represented by the equation (41) and also by using nonassociated plasticity models Φ_{sd} (Rudnicki & Rice, 1975). The discussion of this topic is beyond the scope of this study and will be dealt with in a forthcoming contribution.

5. Analysis of Pore Collapse and Shear-Enhanced Compaction

Analysis of pore collapse and shear-enhanced compaction is complex owing to the nonlinear behavior of reservoir rocks (Smits et al., 1988; Boade et al., 1989). To analyze these phenomena, the poro-elastoplastic coupling with considering the nonlinear Davies permeability model is proposed. The following numerical models are developed, such as: (1) homogeneous stress state of hydrostatic and triaxial test, (2) two-dimensional model of horizontal wellbore drilling, (3) two-dimensional model of horizontal well production, (4) subsidence in a three-dimensional model of reservoir with horizontal production well.

5.1. Hydrostatic and Triaxial Compression Test

The pore collapse and shear-enhanced compaction are analyzed numerically by implementing a hydrostatic and triaxial compression test, respectively. The numerical models are done using a homogeneous stress states. The material properties for the hydrostatic and triaxial test are given in Table 1. The evolution of loading applied on the sample to reach the final stresses in 20 states is given in Table 2. Figure 5 is representative of the equivalent loading condition. The hydrostatic and triaxial loading conditions are as follows:

- The hydrostatic test is modeled in a stress-rate control where a confining stress σ_c is applied at the top and right side of sample and zero normal displacements on the two other boundaries. The stress ratio k_s is the ratio of horizontal stress to vertical stress, is equal 1.0. Moreover, a fixed pressure 1 MPa is applied above the top and right side of sample and impermeable wall on two other sides.

- The triaxial test is modeled in a stress-rate control where an axial total stress σ_a is applied at the top of sample and a constant confinement stress σ_c is applied on the right side of sample and zero normal displacement is imposed on the two other boundaries. The stress ratio k_s for triaxial test is equal to 0.5, where $k_s = \sigma_c/\sigma_a = 0.5$. Moreover, a fixed pressure 1 MPa is applied at the top and right side of sample and an impermeable wall is modeled to the two other sides.

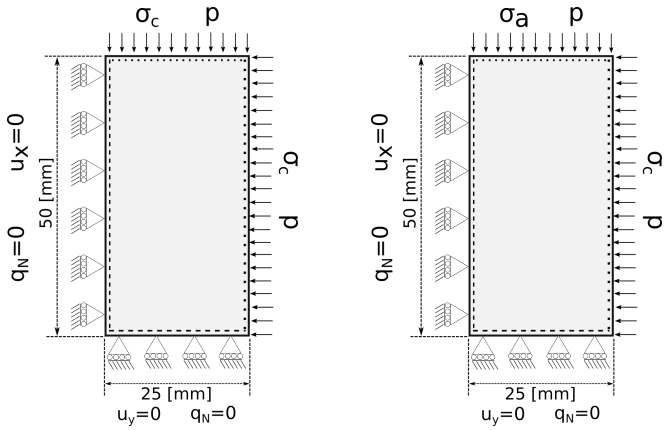

Figure 5. Domain of: (left) hydrostatic test , and (right) triaxial test.

Parameter	Variable [unit]	Value
Young's modulus	E MPa	2800.0
Poisson's ratio	ν	0.2
Biot coefficient	α	1
Fluid compressibility	c_f MPa^{-1}	0
Fluid dynamic viscosity	η Pa s	1×10^{-3}
Initial porosity	ϕ°	0.1
Initial Abs. permeability	κ° m^2	1×10^{-13}
Permeability coefficient	$\mathcal{Z}$	30.0
A	MPa	18.0
B	MPa^{-1}	0.01
C	MPa	14.0
D	MPa^{-1}	0.0065
W		0.025
R		3.0
$X_{\circ}$	MPa	-25.0

Table 1. Material parameters employed for the hydrostatic and triaxial test.

Num. step	σ_a	σ_c in hydrostatic	σ_c in triaxial
	MPa	MPa	MPa
0	−1.0	−1.0	-1.0
1	−1.0	−1.0	-1.0
2	−2.0	−2.0	-1.0
3	−3.0	−3.0	-1.5
4	−4.0	−4.0	-2.0
5	−5.0	−5.0	-2.5
6	−6.0	−6.0	-3.0
7	−7.0	−7.0	-3.5
8	−8.0	−8.0	-4.0
9	−9.0	−9.0	-4.5
10	−10.0	−10.0	-5.0
11	−11.0	−11.0	-5.5
12	−12.0	−12.0	-6.0
13	−13.0	−13.0	-6.5
14	−14.0	−14.0	-7.0
15	−15.0	−15.0	-7.5
16	−16.0	−16.0	-8.0
17	−17.0	−17.0	-8.5
18	−18.0	−18.0	-9.0
19	−19.0	−19.0	-9.5
20	−20.0	−20.0	-10.0

Table 2. The axial and lateral stresses applied to the sample for hydrostatic and triaxial test.

To analyze the pore collapse and shear enhanced compaction, the results of a material point subject to evolving stresses is studied. By applying the axial and lateral stresses to the sample, the deformation of the sample is increased. The numerical results in Figure 6 (left) indicate the onset of pore collapse and shear-enhanced compaction where the plastic volumetric strain begins. The results demonstrate that the onset of pore collapse is $P^* = 4.96\,\text{MPa}$ and shear-enhanced compaction is $C^* = 4.38\,\text{MPa}$.

In Figure 6 (middle), the capability of DiMaggio-Sandler cap function to capture pore collapse P^* and shear-enhanced compaction C^* is displayed. It means the cap surface can present the onset of pore collapse under hydrostatic condition and shear-enhanced compaction under triaxial condition. In addition, it can apply for any path stress data to understand whether these phenomena may occur or not.

Figure 6 (right) demonstrates clearly the shear-enhanced compaction by expressing the quantities of β_p where the sign of them are negative (according

to the Wong compaction model). The value of β_p becomes negative when the compaction plastic strain starts: it implies the onset of shear-enhanced compaction. This process is repeated for pore collapse and the results are presented in Figure 6 (middle-right). Moreover, the position of the μ/β points resulting from the simulation are plotted and compared with the shear bands proposed by Rudnicki & Rice (1975) in equation (40). One can observe that, using the DiMaggio plastic parameters, the points are moving towards shear enhanced compaction band, but their position would not indicate a critical value.

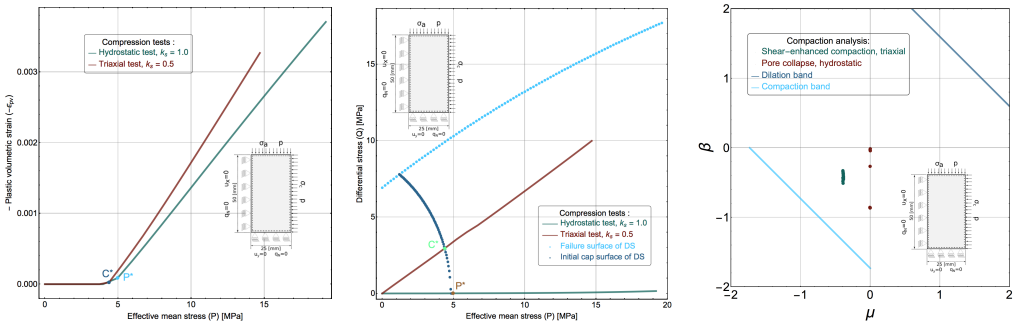

Figure 6. Numerical results of hydrostatic and triaxial test: (left) the relation between mean effective stress and plastic volumetric strain, (middle) capability of DiMaggio-Sandler cap function to capture pore collapse and shear-enhanced compaction, (right) shear bands region.

The results of Figure 6 present that the numerical modeling can indicate the onset of pore collapse and shear-enhanced compaction. In addition, the numerical results show that the evolution of pore collapse (post-pore collapse) and shear-enhanced compaction (post-shear enhanced compaction) can be simulated using the hardening function of DiMaggio-Sandler model.

In this study, the effect of pore collapse and shear-enhanced compaction on porosity and permeability numerically are analyzed. The relation between porosity and effective mean stress is shown in Figure 7 (left) and the relation between permeability and effective mean stress is displayed in Figure 7 (right).

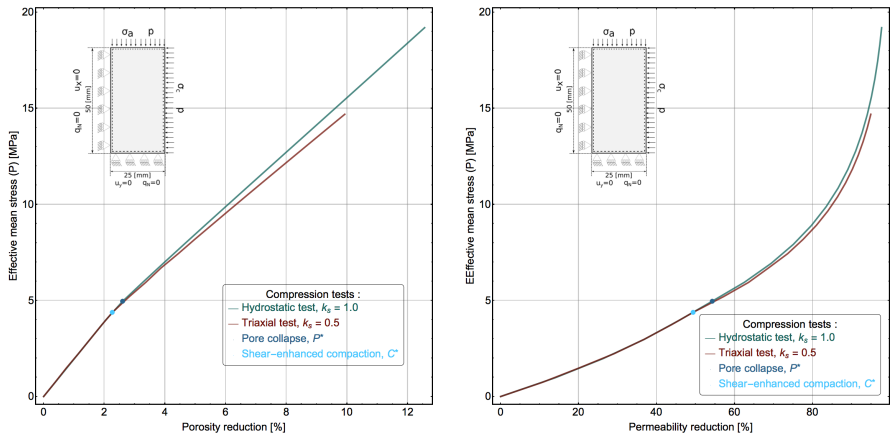

Figure 7. Numerical modeling of hydrostatic and triaxial test to see the effect of pore collapse and shear-enhanced compaction on: (left) porosity and (right) permeability.

The results of Figure 7 emphasize that by increasing effective mean stress, the quantity of porosity and permeability are decreased and the reduction of porosity and permeability are irreversible when the onset of pore collapse and permeability is initiated. Moreover, the results indicate that the coupling of poro-elastoplasticity and permeability can describe the pore collapse and shear-enhanced compaction and their effects on the change of porosity and permeability.

5.2. Two-dimensional model of horizontal wellbore drilling

The study of pore collapse and shear-enhanced compaction during wellbore drilling is numerically conducted. The numerical approximation is implemented using continuous finite element approximations for rock deformation and Raviart-Thomas mixed finite element approximation for pore pressure and flux. The numerical modelling are implemented under hydrostatic and triaxial far field loading conditions. For the hydrostatic loading $k_s = 1.0$, the in-situ vertical stress is $\sigma_v = 60$ and the in-situ horizontal stress is $\sigma_h = \sigma_H = 60$ MPa. For the triaxial loading $k_s = 0.9$, the in-situ vertical stress is $\sigma_v = 60$ and the in-situ horizontal stress is $\sigma_h = \sigma_H = 54$ MPa. The initial or far-field pore pressure is $p^\circ = 45$ MPa. To analyze the impact of pore collapse and shear-enhanced compaction on horizontal wellbore drilling, a *2D* numerical model is implemented (see in Figure 11). The numerical mesh is composed of quadratic polynomial order elements for displacement and linear Raviart Thomas flux/pore pressure pairs for the fluid

approximation. This combination of finite element approximations satisfies the LBB inf-sup condition. The size of the computational domain is 20×20 [m] in the h and v directions, respectively. The radius of horizontal well is $r_w = 0.1\,\mathrm{m}$.

The numerical simulation is performed as follows. First, the initial homogeneous stress/pressure state of the reservoir is imposed as the in-situ stress and initial pore pressure.Next, the mud pressure is applied from $p_m = 45.0$ MPa to $p_m = 40.0$ MPa over 11 steps. The relation among in-situ stress $\boldsymbol{\sigma}_t$, effective stress $\boldsymbol{\sigma}$, and mud pressure p_m is $\boldsymbol{\sigma}_t = \boldsymbol{\sigma} - \alpha p_m \mathbf{I}$. The mud pressure evolution is documented in Table 3. The model parameters are given in Table 4.

Num. step	Mud pressure p_m MPa
0	45.0
1	45.0
2	44.5
3	44.0
4	43.5
5	43.0
6	42.5
7	42.0
8	41.5
9	41.0
10	40.5
11	40.0

Table 3. A mud pressure evolution for horizontal wellbore drilling.

Parameter	Value	Variable [unit]
Young's modulus	3800.0	E MPa
Poisson's ratio	0.2	ν
Biot's coefficient	1.0	α
Fluid compressibility	0	c_f MPa^{-1}
Fluid dynamic viscosity	1×10^{-3}	η Pa s
Initial porosity	0.1	ϕ°
Initial Abs. permeability	1×10^{-13}	κ° m^2
Permeability coefficient	30.0	$\mathcal{Z}$
A	50.0	MPa
B	0.028	MPa^{-1}
C	40.0	MPa
D	0.001	MPa^{-1}
W	0.002	
R	3.0	
$X_{\circ}$	-72.0	MPa

Table 4. Material parameters for *2D* model horizontal wellbore drilling.

To analyze the onset of pore collapse and shear-enhanced compaction on wellbore drilling, the data point around the wellbore region, namely $pt_w = (x = 0.085\text{m}, y = 0.085\text{m})$ and $||pt_w|| = 0.12$ is selected. By applying the vertical and horizontal stresses to the wellbore, as given in Table 3, the effective stress and consequently the deformation near to the wellbore is increased. Then, the relation between mean effective stress and plastic volumetric strain is shown in Figure 8 (left), in which the onset of pore collapse and shear-enhanced compaction is where the plastic volumetric strain begins and the quantity of plastic volumetric strain is not equal zero. It is required to mention that the initial mud pressure is equal to the initial pore pressure, namely $p^{\circ} = 45$, thus the initial effective stress is not equal zero due to the difference between in-situ stress $\boldsymbol{\sigma}_t$ and mud pressure p_m, i.e., $\boldsymbol{\sigma} = \boldsymbol{\sigma}_t + \alpha p_m \mathbf{I}$. In addition, the big step in the Figure 8 (left) can be because of the opening of wellbore.

The numerical results in Figure 8 (left) indicate that the onset of pore collapse is $P^* = 15.64$MPa and the shear-enhanced compaction is $C^* = 12.57$MPa. In Figure 8 (middle), the capability of DiMaggio-Sandler cap function to capture pore collapse P^* and shear-enhanced compaction C^* is

illustrated. In Figure 8 (right), according to the Wong's compaction model, the pore collapse and shear-enhanced compaction are occurring during horizontal wellbore drilling due to the negative quantities of β_p, which are computed using equation (39). Moreover, the shear bands provided by Rudnicki & Rice (1975) in equation (40) are displayed in this figure.

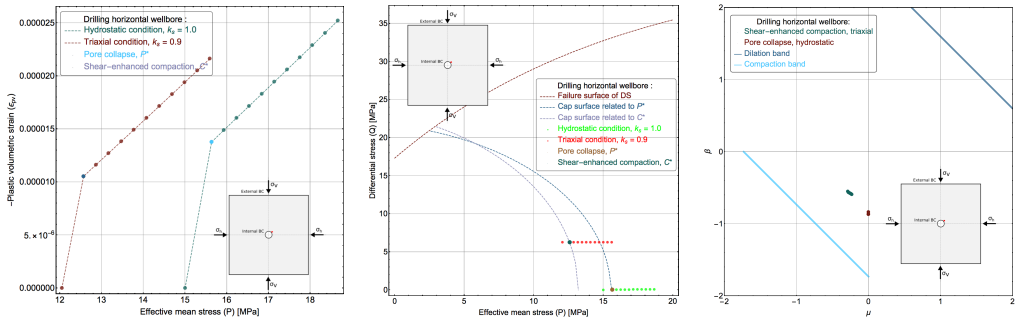

Figure 8. The results of wellbore drilling: (left) the relation between mean effective stress and plastic volumetric strain, (middle) capability of DiMaggio-Sandler cap function to capture pore collapse and shear-enhanced compaction, (right) shear bands region.

The results of Figures 8 illustrate that, according to the DiMaggio Sandler model, the onset of pore collapse and shear-enhanced compaction can occur during horizontal wellbore drilling. Moreover, it can be observed that stress points are closer to pore collapse than shear enhanced compaction.

Previous studies (Heiland, 2003; Jongerius, 2016) indicate that the onset and post-pore collapse and shear-enhanced compaction have an effect on petrophysical properties, such as porosity and permeability. This motivates the numerical evaluation of the impact of pore collapse and shear-enhanced compaction on porosity and permeability. Figure 9 (left) shows the relation between porosity reduction and effective mean stress. The results confirm the reduction of the porosity when the effective mean stress is increased. Figure 9 (right) illustrates the relation between permeability reduction and effective mean stress, where the permeability decreases with increasing the effective mean stress.

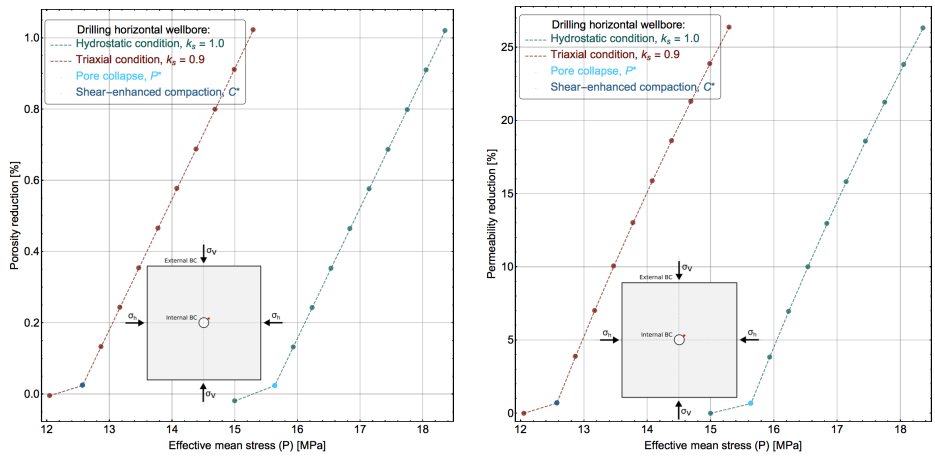

Figure 9. Numerical modeling of horizontal wellbore drilling: (left) porosity reduction and (right) permeability reduction.

The distribution of porosity and permeability under hydrostatic condition is illustrated in Figure 10 (left) and (right), respectively.

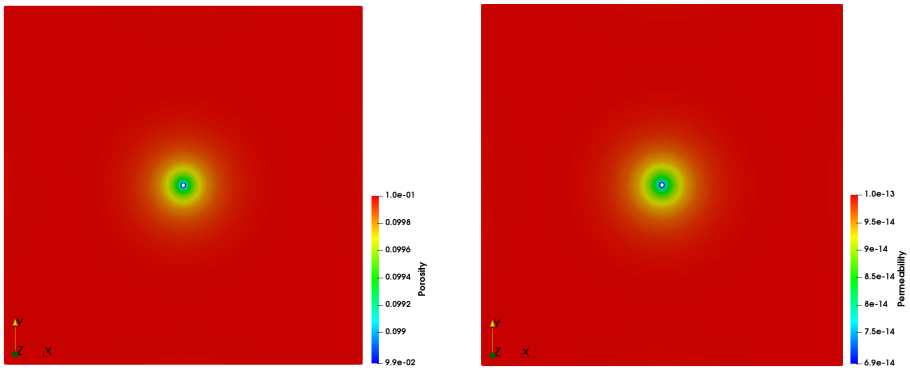

Figure 10. Numerical modeling of horizontal wellbore drilling: (left) distribution of porosity under hydrostatic condition, and (right) distribution of permeability under hydrostatic condition at $p_m = 40.0$ [MPa].

5.3. Two-dimensional model of horizontal well production

As many horizontal wells have open-hole completions, open-hole stability analysis is required for the safe and economic production (Zhang et al., 2006). To consider the impact of pore collapse and shear-enhanced compaction on well production, a *2D* numerical model of a horizontal well in open-hole completion is implemented (see in Figure 11). The numerical approximation is

implemented using continuous finite element approximations for rock deformation and Raviart-Thomas mixed finite element approximation for pore pressure and flux. The numerical mesh is performed using quadratic polynomial order for displacement and linear polynomial order for flux and pore pressure. The numerical simulations include both hydrostatic and triaxial loading conditions. For the hydrostatic loading (i.e. $k_s = 1.0$), the in-situ vertical stress is 60.0 MPa and the in-situ horizontal stress is 60.0 MPa. For the triaxial loading (i.e. $k_s = 0.8$), the in-situ vertical stress is 60.0 MPa and the in-situ horizontal stress is 48.0 MPa. The size of the computational domain is 20×20 [m] in the h and v directions, respectively. The radius of well is $r_w = 0.1\,\mathrm{m}$.

The simulation is conducted as follows. First, the initial state of the reservoir is computed based on the pore pressure of 40.0 MPa and the in-situ stress is imposed on both on the well and the far field boundaries of the domain. Next, the stress applied at the wellbore is changed stepwise from the in situ state stress to the reservoir pressure of 40.0 MPa to simulate the open-hole completion. Finally, the wellbore pressure is decreased to 22.0 MPa over a time span of 10 [d]. The pressure evolution is documented in Table 5. The model parameters are given in Table 6.

Num. step	Time d	Well pressure MPa
0	0.0	40.0
1	1.0	40.0
2	2.0	38.0
3	3.0	36.0
4	4.0	34.0
5	5.0	32.0
6	6.0	30.0
7	7.0	28.0
8	8.0	26.0
9	9.0	24.0
10	10.0	22.0

Table 5. A series of decreasing wellbore pressure for horizontal well production.

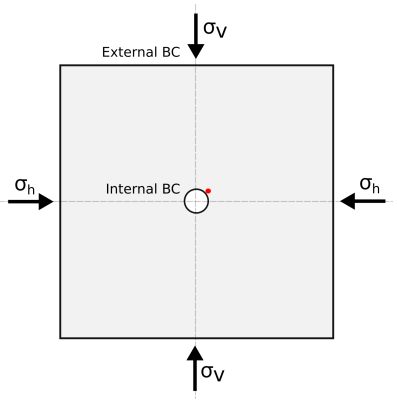

Figure 11. States of in-situ stress for horizontal well.

Parameter	Value	Variable [unit]
Young's modulus	4000.0	E MPa
Poisson's ratio	0.2	ν
Biot's coefficient	1	α
Fluid compressibility	0	c_f MPa^{-1}
Fluid dynamic viscosity	1×10^{-3}	η Pa s
Initial porosity	0.1	ϕ°
Initial Abs. permeability	1×10^{-13}	κ° m^2
Permeability coefficient	30.0	$\mathcal{Z}$
A	50.0	MPa
B	0.028	MPa^{-1}
C	40.0	MPa
D	0.001	MPa^{-1}
W	0.002	
R	3.0	
$X_{\circ}$	-65.0	MPa

Table 6. Material parameters for *2D* model of horizontal well production.

To analyze the onset of pore collapse and shear-enhanced compaction in the horizontal well production, a data point around the wellbore region, namely $pt_w = (x = 0.085\mathrm{m}, y = 0.085\mathrm{m})$ and $||pt_w|| = 0.12\mathrm{m}$ is selected.

The left graph in Figure 12 shows that the onset of pore collapse and shear-enhanced compaction where the plastic volumetric strain begins. The

results indicate that the onset of pore collapse is $P^* = 1.26\,\text{MPa}$ and the shear-enhanced compaction is $C^* = 1.24\,\text{MPa}$.

In Figure 12 (middle), the capability of DiMaggio-Sandler cap model to capture and present the onset of pore collapse P^* and shear-enhanced compaction C^* is illustrated. In Figure 12 (right), according to the Wong's model, the compaction phenomenon, namely pore collapse and shear-enhanced compaction occurs in horizontal well due to the negative quantities of β_p which are calculated using equation (39). Moreover, the shear bands expressed by Rudnicki & Rice (1975) in equation (40) are presented in this figure.

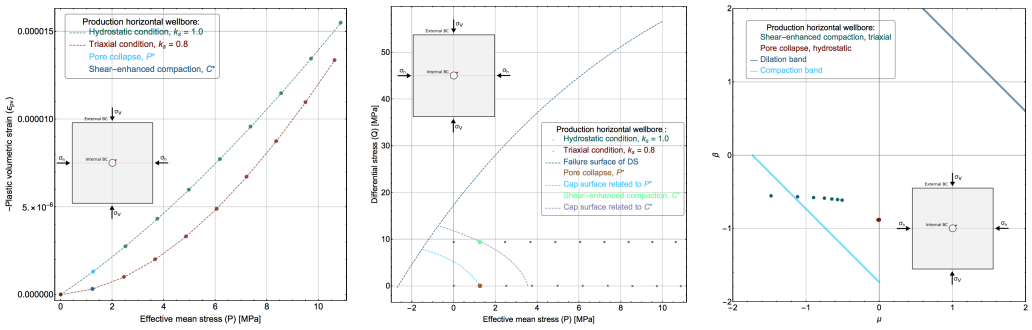

Figure 12. The numerical results of a horizontal well production for a total time span of 10.0 [d] by considering the time step size is 1.0 [d]: (left) the relation between mean effective stress and plastic volumetric strain, (middle) capability of DiMaggio-Sandler cap function to capture pore collapse and shear-enhanced compaction, and (right) shear bands region.

The results of Figure 12 present that if the material can be modeled by DiMaggio Sandler plasticity the onset and evolution of pore collapse and shear-enhanced compaction will occur during well production.

Previous study (Heiland, 2003; Jongerius, 2016), emphasize that the onset and evolution of both pore collapse and shear-enhanced compaction have an influence on petrophysical properties such as porosity and permeability. In this study, the effect of pore collapse and shear-enhanced compaction on the porosity and permeability and, consequently production, are analyzed.

Figure 13 (left) presents the relation between porosity reduction and effective mean stress, in which the results display that the porosity is decreased by increasing the effective mean stress. Figure 13 (middle) illustrates the relation between permeability reduction and effective mean stress, in which the results show that the permeability is reduced by increasing the effective mean stress.

Figure 13 (right) indicates the relation between flux and effective mean stress, in which the results display that the flux is decreased by increasing an effective mean stress. Thus, the change of flux leads to change the quantity of mass extracted from the system.

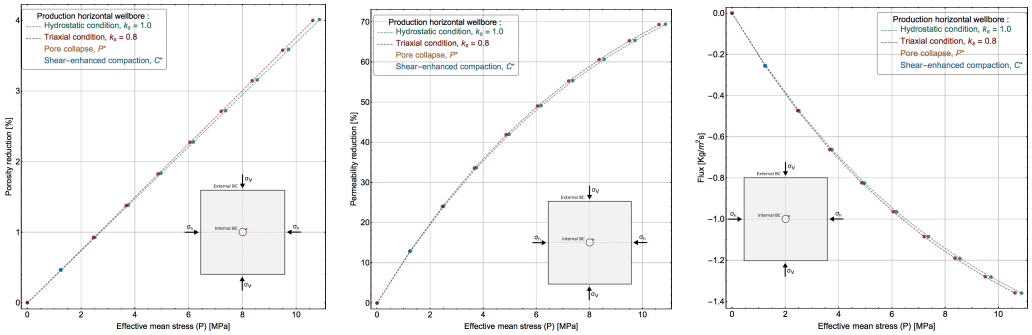

Figure 13. Numerical modeling of a horizontal well production: (left-top) porosity reduction, (middle-top) permeability reduction, (right-top) the relation between flux and effective mean stress.

The distribution of porosity and permeability under hydrostatic condition are illustrated in Figure 14 (left) and (right), respectively.

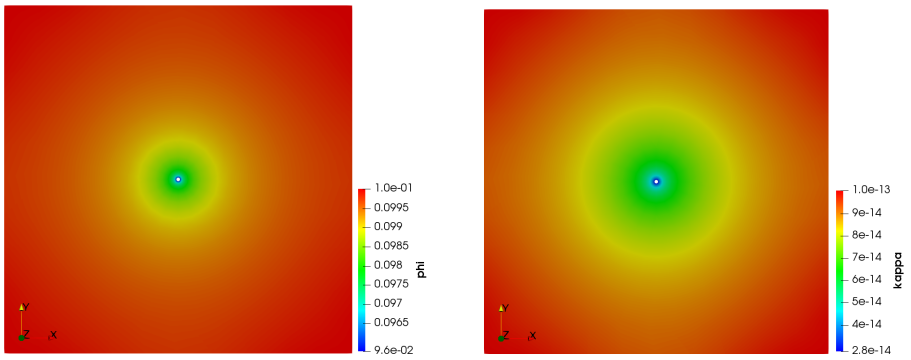

Figure 14. Numerical modeling of a horizontal well production: (left) distribution of porosity under hydrostatic condition, and (right) distribution of permeability under hydrostatic condition at $p_w = 22.0$ [MPa].

The numerical results of Figure 13 emphasize that by increasing effective mean stress, the quantity of porosity and permeability are decreased and the reduction of porosity and permeability are irreversible when the onset of pore collapse and permeability is begone.

5.4. Subsidence in a 3D Reservoir with Horizontal Production Well

In this subsection, the numerical modelling of a *3D* reservoir with a horizontal production well in open-hole completion is implemented. The length, width and height of the model are 50m, 20m and 20m and the radius of well is 0.1 m. The numerical approximation is implemented using continuous finite element approximations for rock deformation and Raviart-Thomas mixed finite element approximation for pore pressure and flux. The simulation is conducted similar to the *2D* production horizontal well and the numerical mesh is performed by quadratic polynomial order for displacement and linear polynomial order for flux and pore pressure. Moreover, the horizontal stress for parallel (σ_Z) and perpendicular (σ_X) to the direction of wellbore are the same, ($\sigma_h = \sigma_X = \sigma_Z$). The material parameters are presented in Table 7. In addition, the simulation is conducted as the same as *2D* production horizontal well.

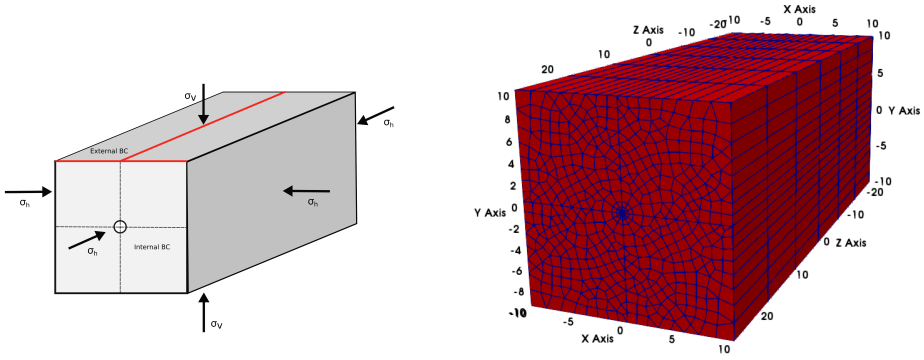

Figure 15. *3D* reservoir with horizontal production well: (left) boundary conditions, (right) graphical representation of the geometry.

Parameter	Value	Variable [unit]
Young's modulus	5000.0	E MPa
Poisson's ratio	0.2	ν
Biot's coefficient	1	α
Fluid compressibility	0	c_f MPa^{-1}
Fluid dynamic viscosity	1×10^{-3}	η Pa s
Initial porosity	0.1	ϕ°
Initial Abs. permeability	1×10^{-13}	κ° m^2
Permeability coefficient	30.0	$\mathcal{Z}$
A	55.0	MPa
B	0.028	MPa^{-1}
C	50.0	MPa
D	0.0001	MPa^{-1}
W	0.0002	
R	3.0	
$X_{\circ}$	-80.0	MPa

Table 7. Parameters employed for a *3D* reservoir with a horizontal production well.

By applying the vertical and horizontal stresses to a *3D* reservoir with an horizontal production well for a total time span of 10.0 [d], as given in Table 6, the deformation near to the horizontal well is increased. The numerical results of all the plots presented in Figure 16 and Figure 17 are reported for two different time values $t = \{1.0, 10.0\}$ [d]. The Figure 16 at top-left position displays the longitudinal subsidence (parallel to the direction of wellbore) and the Figure at top-right presents transverse subsidence (perpendicular to the direction of wellbore). It can be seen that from Figure 16 the effect of vertical stress on the subsidence triggered by the reservoir pressure change. The plot is rendered at the reservoir top. The Figure 16 at bottom-left position presents the longitudinal porosity change and at bottom-right position presents the transverse porosity change due to pressure drop. It can be seen, that the porosity decreases with increasing the reservoir compaction.

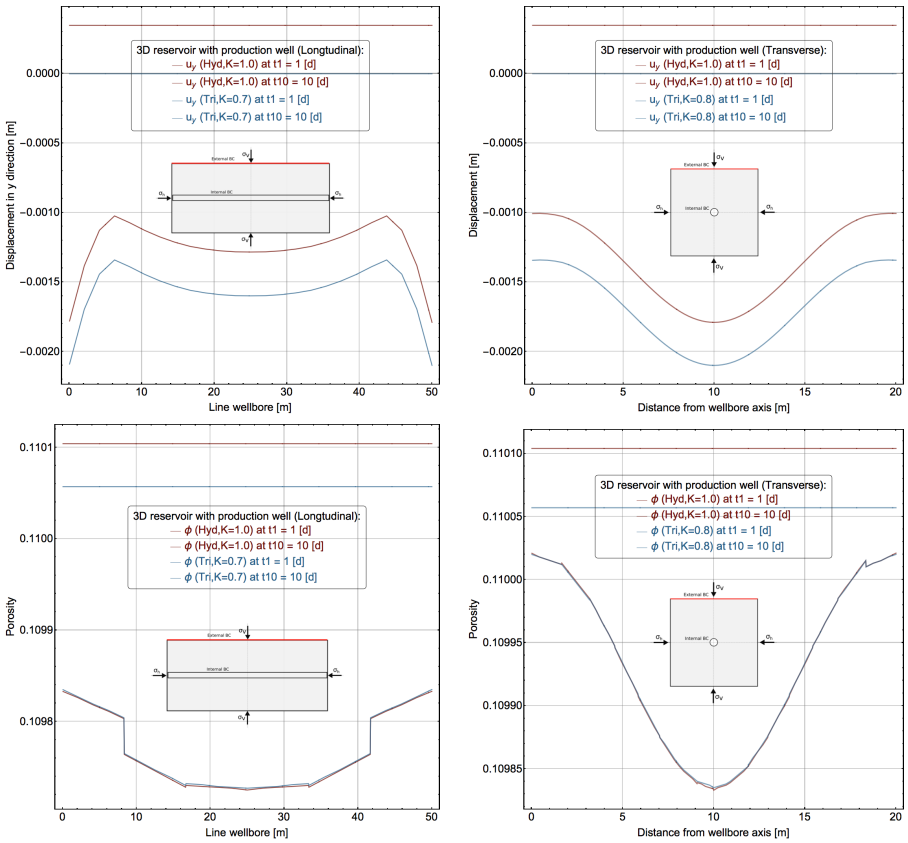

Figure 16. *3D* reservoir with horizontal production well. (top-left) longitudinal displacement, (top-right) transverse displacement, (bottom-left) longitudinal porosity, and (bottom-right) transverse porosity.

The Figure 17 at top-left position presents the longitudinal permeability change and at top-right position presents transverse permeability change due to pressure drop while vertical total stress σ_v is kept constant along the simulation time. The figure allows to understand that the permeability decreases with increasing the reservoir compaction. The Figure 17 at bottom-left and bottom-right position show the variation of radial flux for both cases.

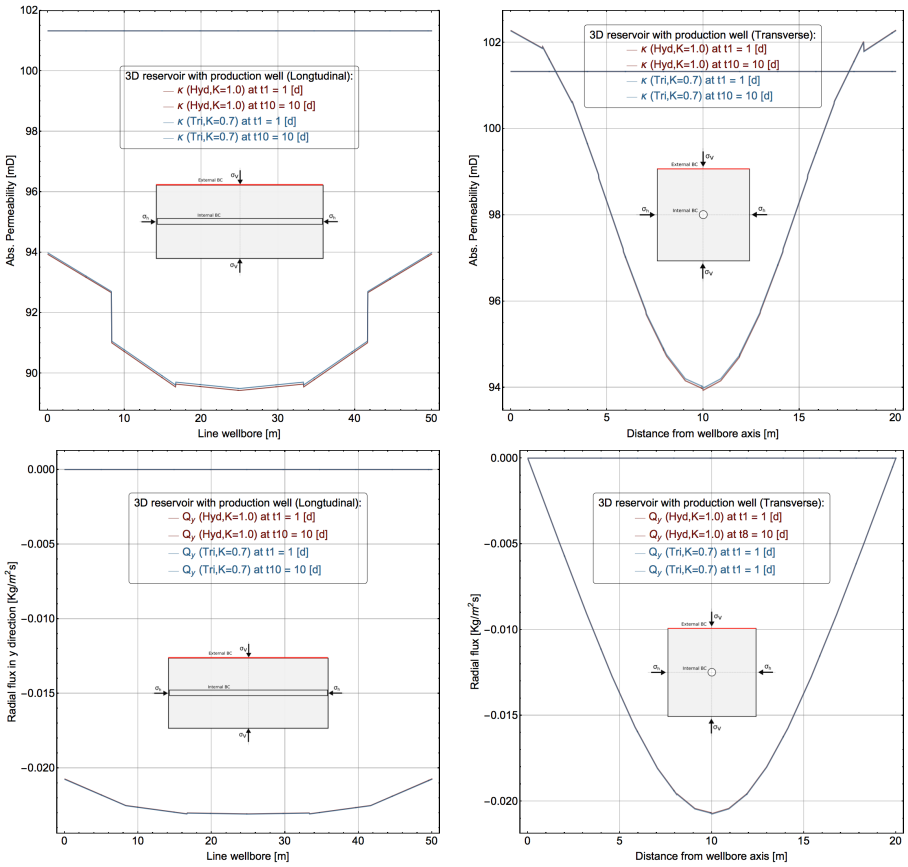

Figure 17. *3D* reservoir with horizontal production well under hydrostatic condition. (top-left) longitudinal permeability, (top-right) transverse permeability, (bottom-left) longitudinal radial flux, and (bottom-right) transverse radial flux.

The Figure 18 at top-left position presents the distribution of displacement under hydrostatic condition, in which the surface subsidence is occurred clearly. The Figure 18 at top-right shows the distribution of porosity under hydrostatic condition where the porosity reduction near to wellbore is because of pressure depletion. The Figure 18 at bottom-left displays the permeability distribution under hydrostatic condition near the wellbore. The Figure 18 at bottom-right shows the radial flux distribution under hydrostatic condition near the wellbore. It can be observed that from only geomechanical effects the wellbore region deteriorates the productivity index associated with the case when is considered a constant permeability and no geomechanical effects.

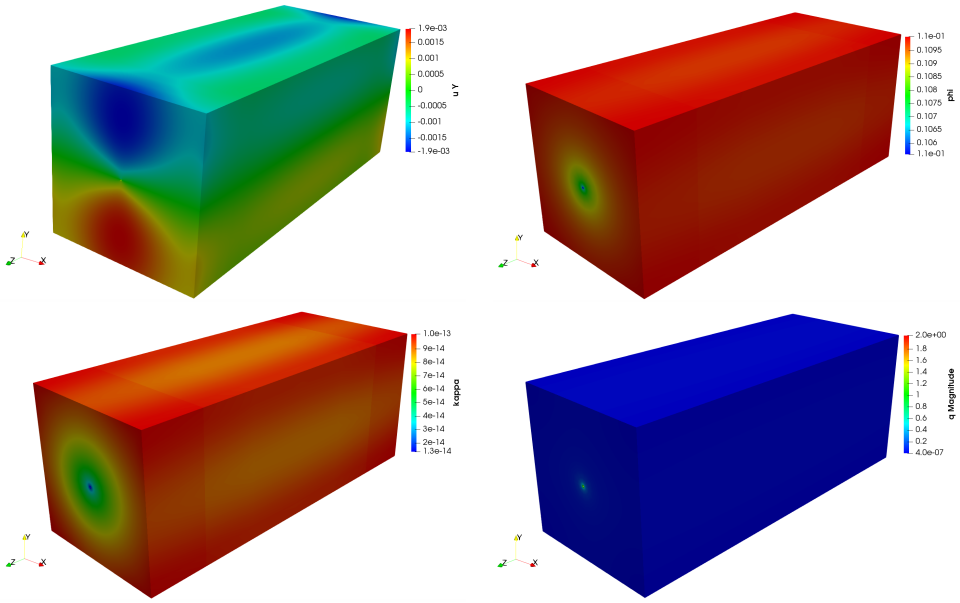

Figure 18. *3D* reservoir with horizontal production well under hydrostatic condition. (top-left) displacement distribution in y direction, (top-right) porosity distribution, (bottom-left) permeability distribution, and (bottom-right) radial flux distribution.

6. Conclusions

The effect of pore collapse and shear-enhanced compaction on the reservoir performance is analyzed using the sequential coupled poro-elastoplasticity and permeability, in which the DiMaggio-Sandler and nonlinear Davies permeability model are used. The onset of pore collapse and shear-enhanced compaction from the numerical results with respect to commonly used approaches is obtained by three methods: firstly using the DiMaggio-Sandler cap plasticity model, second the compaction model of Wong, and third the shear bands of Rudnicki. The numerical results demonstrate that the onset of pore collapse and shear-enhanced compaction is clear, where the plastic volumetric strain begins. The effect of pore collapse and shear-enhanced compaction on porosity and permeability is analyzed, in which by increasing the effective stress, the reduction of porosity and permeability increase. The results demonstrate that while the pore collapse and shear-enhanced compaction are accrued, the change of variables will be irreversible. It means, the deformation is irreversible and consequently the lost of porosity and permeability is irreversible. This change also appear for radial flux of reservoir.

In addition, the numerical results emphasize the importance of in-situ stress ratio k_s on petrophysical properties of reservoir.

7. Acknowledgements

The authors M. Sanei, O. Durán, P.R.B. Devloo thankfully acknowledge financial support from ANP-Brazilian National Agency of Petroleum, Natural Gas and Biofuels (ANP-PETROBRAS) (grant 2014/00090-2). P.R.B. Devloo also acknowledges financial support from FAPESP, Brazil - Fundação de Amparo à Pesquisa do Estado de São Paulo, Brazil (grant 2017/15736-3), and from CNPq - Conselho Nacional de Desenvolvimento Científico e Tecnológico (grant 310369/2006-1). The data supporting our work are provided in the *Zenodo* database by the following DOI: 10.5281/zenodo.3874980.

8. References

A. Schofield, P. W. (1968). Critical state soil mechanics. *Cambridge University Press*.

Abdulraheem, A., Zaman, M., & Roegiers, J.-C. (1994). A finite-element model for ekofisk field subsidence. *Journal of Petroleum Science and Engineering*, 10(4), 299–310.

Addis, M. (1987). Material metastability in weakly cemented sedimentary rocks. *Mem. Geol. Sot. China*, (pp. 495–512).

Addis, M. & Jones, M. E. (1990). Mechanical behavior and strain rate dependence of high porosity chalk, chalk, ed. t. telford. *Mechanical Properties, London*, (17), 239–244.

A.F., F. & J.T., F. (2000). Cap plasticity models and compactive and dilatant pre-failure deformation. *American Rock Mechanics Association*.

Armero, F. & Simo, J. C. (1992). A new unconditionally stable fractional step method for non-linear coupled thermomechanical problems. *International Journal for Numerical Methods in Engineering*, 35(4), 737–766.

Baud, P., Vajdova, V., & fong Wong, T. (2006). Shear-enhanced compaction and strain localization: Inelastic deformation and constitutive modeling of four porous sandstones. *Journal of Geophysical Research: Solid Earth*, 111(B12), n/a–n/a.

Bernard, X. D., Eichhubl, P., & Aydin, A. (2002). Dilation bands: A new form of localized failure in granular media. *Geophysical Research Letters*, 29(24), 29–1–29–4.

Bevillon, D. & Masson, R. (2000). Stability and convergence analysis of partially coupled schemes for geomechanical-reservoir simulations. In *EC-MOR VII - 7th European Conference on the Mathematics of Oil Recovery*: EAGE Publications BV.

Biot, M. & Willis, D. (1957). The elastic coefficients of the theory of consolidation. *J Appl. Mech.*, (pp. 594–601).

Biot, M. A. (1941a). Consolidation settlement under a rectangular load distribution. *Journal of Applied Physics*, 12(5), 426–430.

Biot, M. A. (1941b). General theory of three-dimensional consolidation. *Journal of Applied Physics*, 12(2), 155–164.

Biot, M. A. (1955). Theory of elasticity and consolidation for a porous anisotropic solid. *Journal of Applied Physics*, 26(2), 182–185.

Biot, M. A. (1962). Mechanics of deformation and acoustic propagation in porous media. *Journal of Applied Physics*, 33(4), 1482–1498.

Biot, M. A. (1973). Nonlinear and semilinear rheology of porous solids. *Journal of Geophysical Research*, 78(23), 4924–4937.

Blanton, T. L. (1981). Deformation of chalk under confining pressure and pore pressure. *Society of Petroleum Engineers Journal*, 21(01), 43–50.

Boade, R., Chin, L., & Siemers, W. (1989). Forecasting of ekofisk reservoir compaction and subsidence by numerical simulation. *Journal of Petroleum Technology*, 41(07), 723–728.

Borja, R. I. & Lee, S. R. (1990). Cam-clay plasticity, part 1: Implicit integration of elasto-plastic constitutive relations. *Computer Methods in Applied Mechanics and Engineering*, 78(1), 49–72.

Brace, W. F. (1978). A note on permeability changes in geologic material due to stress. *Pure and Applied Geophysics PAGEOPH*, 116(4-5), 627–633.

Bui, T. A., Wong, H., Deleruyelle, F., Zhou, A., & Lei, X. (2016). A coupled poroplastic damage model accounting for cracking effects on both hydraulic and mechanical properties of unsaturated media. *International Journal for Numerical and Analytical Methods in Geomechanics*, 40(5), 625–650.

Cecílio, D. L., Devloo, P. R., Gomes, S. M., dos Santos, E. R., & Shauer, N. (2015). An improved numerical integration algorithm for elastoplastic constitutive equations. *Computers and Geotechnics*, 64, 1–9.

Chen, W. (1984). Soil mechanics, plasticity and landslides. In *Mechanics of Material Behavior - The Daniel C. Drucker Anniversary Volume* (pp. 31–58). Elsevier.

Coelho, L., S. A. E. N. A. J. L. L. (2003). Modelagem numérica do colapso de poros em rochas carbonáaticas. In *2 Congresson Brasileiro de P&D em PETRÓLEO & GÁS*: Offshore Technology Conference.

Coussy, O. (1989). A general theory of thermoporoelastoplasticity for saturated porous materials. *Transport in Porous Media*, 4(3).

Coussy, O. (1995). *Mechanics of Porous Continua*. Wiley.

Coussy, O. (2004). *Poromechanics*. Wiley.

Curran, J. H. & Carroll, M. M. (1979). Shear stress enhancement of void compaction. *Journal of Geophysical Research*, 84(B3), 1105.

da Silva, R., Murad, M., & Obregon, J. (2018). A new fixed-stress split scheme in poroplastic media incorporating general plastic porosity constitutive theories. In *ECMOR XVI - 16th European Conference on the Mathematics of Oil Recovery*: EAGE Publications BV.

Davies, J. & Davies, D. (1999). Stress-dependent permeability: Characterization and modeling. In *SPE Annual Technical Conference and Exhibition*: Society of Petroleum Engineers.

Davis, R. O. & Selvadurai, A. P. S. (2002). *Plasticity and Geomechanics*. Cambridge University Press.

de Souza Neto, E. A., Peri, D., & Owen, D. R. J. (2008). *Computational Methods for Plasticity*. John Wiley Sons, Ltd.

Dean, R. H., Gai, X., Stone, C. M., & Minkoff, S. E. (2006). A comparison of techniques for coupling porous flow and geomechanics. *SPE Journal*, 11(01), 132–140.

Devloo, P. R. B. (1997). PZ: An object oriented environment for scientific programming. *Computer Methods in Applied Mechanics and Engineering*, 150(1-4), 133–153.

Devloo, P. R. B. (2000). Object oriented tools for scientific computing. *Engineering with Computers*, 16(1), 63–72.

DiMaggio, F. & Sandler, I. (1971). Material model for granular soils. *Journal of the Engineering Mechanics Division*, 97, 935–950.

Duŕan, O., Sanei, M., Devloo, P., & Santos, E. (2019). An enhanced sequential fully implicit scheme for reservoir geomechanics. *Computer and Geoscience*.

Fossum, A., Senseny, P., Pfeifle, T., & Mellegard, K. (1995). Experimental determination of probability distributions for parameters of a salem limestone cap plasticity model. *Mechanics of Materials*, 21(2), 119–137.

Gurevich, A. E. & Chilingarian, G. V. (1993). Subsidence over producing oil and gas fields, and gas leakage to the surface. *Journal of Petroleum Science and Engineering*, 9(3), 239–250.

Gutierrez, M. S. & Lewis, R. W. (2002). Coupling of fluid flow and deformation in underground formations. *Journal of Engineering Mechanics*, 128(7), 779–787.

Heiland, J. (2003). Laboratory testing of coupled hydro-mechanical processes during rock deformation. *Hydrogeology Journal*, 11(1), 122–141.

Hoek, E. (2016). *Surface and Underground Project Case Histories: Comprehensive Rock Engineering: Principles, Practice and Projects*. Pergamon.

Jha, B. & Juanes, R. (2007). A locally conservative finite element framework for the simulation of coupled flow and reservoir geomechanics. *Acta Geotechnica*, 2(3), 139–153.

Jiang, J. & Tchelepi, H. A. (2018). Nonlinear acceleration of sequential fully implicit (sfi) method for coupled flow and transport in porous media.

Jiang, J. & Yang, J. (2018). Coupled fluid flow and geomechanics modeling of stress-sensitive production behavior in fractured shale gas reservoirs. *International Journal of Rock Mechanics and Mining Sciences*, 101, 1–12.

Johnson, J., Rhett, D., & Siemers, W. (1988). Rock mechanics of the ekofisk reservoir in the evaluation of subsidence. In *Offshore Technology Conference*: Offshore Technology Conference.

Jongerius, M. (2016). Reservoir compaction in shallow gas reservoirs: The impact of production-induced reservoir compaction on the recovery of gas from shallow reservoirs.

Karner, S. L., Chester, J. S., Chester, F. M., Kronenberg, A. K., & Hajash, A. (2005). Laboratory deformation of granular quartz sand: Implications for the burial of clastic rocks. *AAPG Bulletin*, 89(5), 603–625.

Kim, J. (2010). *Sequential Methods for Coupled Geomechanics and Multiphase Flow*. PhD thesis, Stanford University. The Department of Energy Resources Engineering.

Kim, J., Sonnenthal, E. L., & Rutqvist, J. (2012). Formulation and sequential numerical algorithms of coupled fluid/heat flow and geomechanics for multiple porosity materials. *International Journal for Numerical Methods in Engineering*, 92(5), 425–456.

Kim, J., Tchelepi, H., & Juanes, R. (2011a). Stability and convergence of sequential methods for coupled flow and geomechanics: Drained and undrained splits. *Computer Methods in Applied Mechanics and Engineering*, 200(23-24), 2094–2116.

Kim, J., Tchelepi, H., & Juanes, R. (2011b). Stability and convergence of sequential methods for coupled flow and geomechanics: Fixed-stress and fixed-strain splits. *Computer Methods in Applied Mechanics and Engineering*, 200(13-16), 1591–1606.

Kim, J., Tchelepi, H. A., & Juanes, R. (2011c). Stability, accuracy, and efficiency of sequential methods for coupled flow and geomechanics. *SPE Journal*, 16(02), 249–262.

Kossa, A. (2011). *Exact stress integration schemes for elastoplasticity*. PhD thesis, Budapest University of Technology and Economics.

Lewis, R. & Schrefler, B. (1998). *The finite element method in the static and dynamic deformation and consolidation of porous media*. John Wiley, New York.

Lewis, R. W., Makurat, A., & Pao, W. K. S. (2003). Fully coupled modeling of seabed subsidence and reservoir compaction of north sea oil fields. *Hydrogeology Journal*, 11(1), 142–161.

Mikelić, A. & Wheeler, M. F. (2012). Convergence of iterative coupling for coupled flow and geomechanics. *Computational Geosciences*, 17(3), 455–461.

Minkoff, S. E., Stoneb, C. M., Bryantc, S., Peszynskac, M., & Wheelerc, M. F. (2003). Coupled fluid flow and geomechanical deformation modeling.

Nguyen, V., Gland, N., Dautriat, J., David, C., Wassermann, J., & Guélard, J. (2014). Compaction, permeability evolution and stress path effects in unconsolidated sand and weakly consolidated sandstone. *International Journal of Rock Mechanics and Mining Sciences*, 67, 226–239.

Ostermeier, R. (2001). Compaction effects on porosity and permeability: Deepwater gulf of mexico turbidite. *Journal of Petroleum Technology*, 53(02), 68–74.

Pan, F. (2009). *Development and application of a coupled geomechanics model for a parallel compositional reservoir simulator*. PhD thesis, UT Austin.

Phillips, P. J. & Wheeler, M. F. (2007). A coupling of mixed and continuous galerkin finite element methods for poroelasticity i: the continuous in time case. *Computational Geosciences*, 11(2), 131–144.

Poulet, T. & Veveakis, M. (2016). A viscoplastic approach for pore collapse in saturated soft rocks using REDBACK: An open-source parallel simulator for rock mEchanics with dissipative feedBACKs. *Computers and Geotechnics*, 74, 211–221.

Rudnicki, J. & Rice, J. (1975). Conditions for the localization of deformation in pressure-sensitive dilatant materials. *Journal of the Mechanics and Physics of Solids*, 23(6), 371–394.

Rudnicki, J. W. (1986). Fluid mass sources and point forces in linear elastic diffusive solids. *Mechanics of Materials*, 5(4), 383–393.

Rutter, E. & Glover, C. (2012). The deformation of porous sandstones; are byerlee friction and the critical state line equivalent? *Journal of Structural Geology*, 44, 129–140.

Samier, P., Onaisi, A., & de Gennaro, S. (2008). A practical iterative scheme for coupling geomechanics with reservoir simulation. *SPE Reservoir Evaluation & Engineering*, 11(05), 892–901.

Sandler, I. S. & Rubin, D. (1979). An algorithm and a modular subroutine for the CAP model. *International Journal for Numerical and Analytical Methods in Geomechanics*, 3(2), 173–186.

Sanei, M., Duran, O., & Devloo, P. R. (2017). Finite element modeling of a nonlinear poromechanic deformation in porous media. In *Proceedings of the XXXVIII Iberian Latin American Congress on Computational Methods in Engineering*: ABMEC Brazilian Association of Computational Methods in Engineering.

Schock, R. N., Heard, H. C., & Stephens, D. R. (1973). Stress-strain behavior of a granodiorite and two graywackes on compression to 20 kilobars. *Journal of Geophysical Research*, 78(26), 5922–5941.

Settari, A. & Mourits, F. (1998). A coupled reservoir and geomechanical simulation system. *SPE Journal*, 3(03), 219–226.

Settari, A. & Walters, D. A. (2001). Advances in coupled geomechanical and reservoir modeling with applications to reservoir compaction. *SPE Journal*, 6(03), 334–342.

Simon, D. E., Coulter, G. R., King, G., & Holman, G. (1982). North sea chalk completions- a laboratory study. *Journal of Petroleum Technology*, 34(11), 2531–2536.

Small, J., Booker, J., & Davis, E. (1976). Elasto-plastic consolidation of soil. *International Journal of Solids and Structures*, 12(6), 431–448.

Smits, R., de Waal, J., & van Kooten, J. (1988). Prediction of abrupt reservoir compaction and surface subsidence caused by pore collapse in carbonates. *SPE Formation Evaluation*, 3(02), 340–346.

Sulak, A. M. & Danielsen, J. (1988). Reservoir aspects of ekofisk subsidence. *Offshore Technology Conference*.

Tembe, S., Baud, P., & fong Wong, T. (2008). Stress conditions for the propagation of discrete compaction bands in porous sandstone. *Journal of Geophysical Research*, 113(B9).

Terzaghi, K. (1925). *Erdbaumechanik auf bodenphysikalischer grundlage*. Franz Deutikle, Leipzig und Wien.

Thomas, L., Chin, L., Pierson, R., & Sylte, J. (2002). Coupled geomechanics and reservoir simulation. In *SPE Annual Technical Conference and Exhibition*: Society of Petroleum Engineers.

Tran, D., Nghiem, L., & Buchanan, L. (2005). Improved iterative coupling of geomechanics with reservoir simulation. In *SPE Reservoir Simulation Symposium*: Society of Petroleum Engineers.

Underhill, J. R. & Woodcock, N. H. (1987). Faulting mechanisms in high-porosity sandstones, new red sandstone, arran, scotland. *Geological Society, London, Special Publications*, 29(1), 91–105.

Vajdova, V., Baud, P., & fong Wong, T. (2004). Compaction, dilatancy, and failure in porous carbonate rocks. *Journal of Geophysical Research: Solid Earth*, 109(B5).

Wan, J. (2002). *Stabilized finite element methods for coupled geomechanics and multiphase flow*. PhD thesis, Stanford university.

Wei, Z. & Zhang, D. (2010). Coupled fluid-flow and geomechanics for triple-porosity/dual-permeability modeling of coalbed methane recovery. *International Journal of Rock Mechanics and Mining Sciences*, 47(8), 1242–1253.

Wheeler, M. F. & Gai, X. (2007). Iteratively coupled mixed and galerkin finite element methods for poro-elasticity. *Numerical Methods for Partial Differential Equations*, 23(4), 785–797.

Wong, T.-F., David, C., & Zhu, W. (1997). The transition from brittle faulting to cataclastic flow in porous sandstones: Mechanical deformation. *Journal of Geophysical Research: Solid Earth*, 102(B2), 3009–3025.

Wong, T.-F., Szeto, H., & Zhang, J. (1992). Effect of loading path and porosity on the failure mode of porous rocks. *Applied Mechanics Reviews*, 45(8), 281.

Xie, S. Y. & Shao, J. F. (2015). An experimental study and constitutive modeling of saturated porous rocks. *Rock Mechanics and Rock Engineering*, 48(1), 223–234.

Xiong, Y., Xu, H., Wang, Y., Zhou, W., Liu, C., & Wang, L. (2018). Fluid flow with compaction and sand production in unconsolidated sandstone reservoir. *Petroleum*, 4(3), 358–363.

Zhang, J., Bai, M., & Roegiers, J.-C. (2006). On drilling directions for optimizing horizontal well stability using a dual-porosity poroelastic approach. *Journal of Petroleum Science and Engineering*, 53(1), 61 – 76.

Zhang, J., Wong, T.-F., & Davis, D. M. (1990). Micromechanics of pressure-induced grain crushing in porous rocks. *Journal of Geophysical Research*, 95(B1), 341.

Zhou, H., Jia, Y., & Shao, J. (2008). A unified elastic–plastic and viscoplastic damage model for quasi-brittle rocks. *International Journal of Rock Mechanics and Mining Sciences*, 45(8), 1237 – 1251.

Zoback, M. D. (2007). *Reservoir Geomechanics*. Cambridge University Press.